2014

Photonic Filtering for Applications in Microwave Generation and Metrology

Marcus Bagnell
University of Central Florida

PHOTONIC FILTERING FOR APPLICATIONS IN MICROWAVE GENERATION AND METROLOGY

by

MARCUS BAGNELL
B.S. University of Florida, 2008
M.S. University of Central Florida 2011

A dissertation submitted in partial fulfillment of the requirements
for the degree of Doctor of Philosophy
in the College of Optics and Photonics
at the University of Central Florida
Orlando, Florida

Fall Term
2014

Major Professor: Peter J. Delfyett

ABSTRACT

This work uses the photonic filtering properties of Fabry-Perot etalons to show improvements in the electrical signals created upon photodetection of the optical signal. First, a method of delay measurement is described which uses multi-heterodyne detection to find correlations in white light signals at 20 km of delay to sub- millimeter resolution. By filtering incoming white light with a Fabry-Perot etalon, the pseudo-periodic signal is suitable for measurement by combining and photodetecting it with an optical frequency comb. In this way, optical data from a large bandwidth can be downconverted and sampled on low frequency electronics.

Second, a high finesse etalon is used as a photonic filter inside an optoelectronic oscillator (OEO). The etalon's narrow filter function allows the OEO loop length to be extremely long for a high oscillator quality factor while still suppressing unwanted modes below the noise floor. The periodic nature of the etalon allows it to be used to generate a wide range of microwave and millimeter-wave tones without degradation of the RF signal.

ACKNOWLEDGMENTS

I would like to thank my colleagues in the ultrafast photonics group for all their support and insightful discussion including Dr. Franklyn Quinlan, Dr. Jim-Yung Kim, Dr. Sarper Ozhahar, Dr. Ibrahim Ozdur, Dr. Dimitrios Mandridis, Dr. Umar Priacha, Dr. Nazanin Hoghoogi, Dr. Josue Davila-Rodriguez, Dr. Charles Williams, Dr. Dat Ngyuen, Dr. Abhijeet Ardey, Sharad Bhooplapur, Edris Sarailou, Anthony Klee, and Kristina Bagnell. I would also like to especially thank my advisor, Dr. Peter Delfyett whose guidance and support were invaluable throughout my time at UCF.

TABLE OF CONTENTS

LIST OF FIGURES

LIST OF ACRONYMS AND ABBREVIATIONS

AOM	Acousto-optic modulator
ASE	Amplified spontaneous emission
BPF	Band pass filter
CW	Continuous wave
dB	Decibel
dBm	Decibel relative to 1 mW
EDFA	Erbium-doped fiber amplifier
FSR	Free spectral range
IM	Intensity modulator
LPF	Low pass filter
MH	Multi-heterodyne
MLL	Mode-locked laser
OEO	Optoelectronic oscillator
PC	Polarization controller
PDH	Pound-Drever-Hall
PID	Proportional-integral-derivative

PM	Phase modulator
RF	Radio frequency
SMF	Single mode fiber
SNR	Signal-to-noise
SOA	Semiconductor optical amplifier
VCO	Voltage controlled oscillator

CHAPTER 1: INTRODUCTION

RF Photonics

The continuing desire for transferring large amounts of data, making more precise measurements of distances both large and small, and making more detailed interrogations of the scientific laws that govern the world around us require corresponding improvements in the tools and techniques used in acquiring the information we seek. Photonic technologies continue to provide improvements in methods to generate and manipulate signals with high a signal-to-noise ratio (SNR) and long term frequency stability.

The development of the optical frequency comb[1] has provided a new tool for use in a wide variety of applications. The mode-locking mechanisms can provide large sets of comb-lines with spacings ranging from a few megahertz to over 100 GHz with equally spaced comb-lines down to one part in 10^{-15}. By referencing a frequency comb to a narrow linewidth, CW laser, the linewidth of each individual comb-line can be narrowed to sub-Hertz levels[2]. Stable frequency combs have applications in analog-to-digital conversion[3], arbitrary waveform generation[4], astronomical spectrograph calibration[5], and for distance measurements ranging from sub-micron to tens of kilometers[6].

Multi-heterodyne (MH) detection is a technique that takes advantage of the narrow linewidth and precise frequency spacing of optical frequency comblines to photodetect and downconvert periodic optical signals into the RF domain for sampling and analysis on low frequency electronic diagnostic equipment. Each combline is used as an independent local oscillator. The narrow linewidth of a combline allows accurate heterodyne detection to record amplitude and phase of the signal and the precise

frequency spacing creates a mapping function for complete reconstruction of the optical signal from the sampled RF data.

This work uses multi-heterodyne detection to record the amplitude and phase of periodically filtered light from a broadband light source. Filtering broadband light through a Fabry-Perot etalon results in a pseudo-periodic waveform which can be sampled with MH detection. The advantage of this method is that portions of the optical spectrum across a very large bandwidth can be downconverted and electronically sampled on low frequency electronics. By recording optical data across 100 GHz of optical spectrum on 8 GHz electronic equipment, correlations of the white light spectrum can be found at 20 km of optical delay to sub-millimeter precision. This technique can be used for distance calibration between widely spaced detectors by using standoff detection of the optical signal of interest.

Optoelectronic oscillators are well-established systems for generating low phase noise, long term stable microwave and millimeter-wave signals for use in communications and metrology[7]. Their ability to generate low phase noise tones is a result of photonic components within the OEO loop, specifically single mode optical fiber with a loss of just 0.2 dB/km. Adding large amounts of fiber delay significantly increases the energy storage within the oscillator, resulting in a high quality factor. Report of an OEO with phase noise of -163 dBc/Hz at 10 kHz offset[8] is currently the lowest phase noise for any oscillator. An OEO's method of delay line signal generation comes with the added expense of oscillating modes, close to the carrier, which occur at multiples of the inverse of the round trip delay within the gain bandwidth of the loop. These spurious modes add significantly to the phase noise, often counteracting the low noise properties gained from a long fiber

delay. Several techniques exist, both electronic and photonic, to filter and suppress these modes.

This work describes experiments which take advantage of a method of photonic filtering using a high finesse, Fabry-Perot etalon to replace the relatively wide-band RF filter within the OEO loop. An etalon with 100,000 finesse is used as a filter to provide several orders of magnitude narrower filtering capability than that available by electronic means. Additionally, the physical stability of the etalon makes it suitable for use as a secondary optical reference to provide a narrow linewidth, long term stable optical reference, further contributing to the low noise properties of the generated microwave and millimeter-wave signals.

CHAPTER 2: MULTI-HETERODYNE DETECTION AND SAMPLING OF WHITE LIGHT

Chapter Introduction

This chapter is divided into three sections. Multi-heterodyne detection of white light combines elements of spectral interferometry and heterodyne interferometry to ultimately take advantages from each technique. Information from broad bandwidth optical signals is recorded and analyzed on low bandwidth equipment. The first section, describes work done using spectral interferometry to characterize dispersion of a quantum dot-based semiconductor optical amplifier for potential use as a mode-locked laser gain medium[9]. The second section, describes preliminary work done with heterodyne interferometry which led, finally to the multi-heterodyne experiments and results described in section three.

Optical Spectral Interferometry

Introduction

Spectral interferometry has been used for group delay characterization of a wide variety of materials[10-12]. The technique uses a Michelson or Mach-Zehnder style interferometer with a broadband light source (Figure 1). The light is divided into a reference beam and another which passes through the device under test. The beams are recombined and the spectral phase is determined by the interference of the beams. Interference can be measured either temporally, with a movable mirror and single photodetector or spectrally, by keeping the relative path length difference static and spatially separating and detecting spectral components with a spectrometer. The static version, used here, has no moving

parts and is preferable under the condition that a spectrometer with sufficient resolution is available.

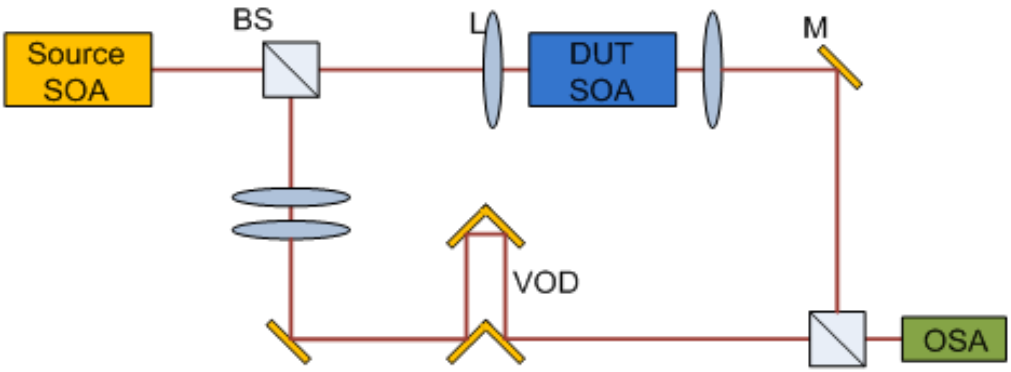

Figure 1. Mach-Zehnder spectral interferometer experimental setup; SOA, semiconductor optical amplifier; DUT, device under test; BS, beam splitter; L, coupling lens; M, mirror; VOD, variable optical delay; OSA, optical spectrum analyzer.

Group Delay of a Quantum Dot Semiconductor Optical Amplifier

Quantum dot-based semiconductor optical amplifiers (SOAs) are attractive for possible use as gain media in broadband mode-locked lasers. Quantum dot SOAs (QD-SOA) have shown wide gain bandwidths, more variability of their linewidth enhancement factor, lower temperature sensitivity, low chirp, and higher modulation bandwidths over devices based on quantum well[13]. The gain bandwidth of a QD-SOA can be greater than 15 THz. This is especially attractive for the generation of broad mode-locked laser spectra with the potential for transform limited pulse widths of less than 100 fs. This capability is desired for many applications in high speed communication and signal processing[14].

SOA gain is controlled by varying the injection current, which also results in a change in the carrier concentration in the active region. The complex index of refraction

of a medium is known to be dependent on the carrier concentration in the medium. Therefore, changing the gain in a laser cavity changes the mode spacing of a mode locked laser. As the SOA gain is often one of the key elements determining both the static and dynamic dispersion of a mode-locked laser, it is important to have a clear understanding of the dependence of the dispersion and its higher order terms on injection current. This information can be used in determining the proper dispersion compensation techniques for broad bandwidth mode-locked laser sources.

Quantifying Dispersion

A Taylor expansion of the propagation constant, β, provides a set of coefficients which is used to quantify the dispersive properties of the SOA. $\beta(\omega)$ is related to the spectral phase by:

$$\beta(\omega) = \frac{\Phi(\omega)}{L} = \frac{\omega/c \cdot n(\omega)}{L}, \tag{1}$$

where $\Phi(\omega)$ is the spectral phase, L is the length of the medium, and n is the frequency dependent refractive index. Taking the first derivative yields:

$$d\beta/d\omega = \frac{d\Phi/d\omega}{L}. \tag{2}$$

This is the group delay over the length of the device, the quantity measured in this work. The expansion of β is

$$\beta = \beta_0 + \beta_1(\omega - \omega_0) + \frac{1}{2!}\beta_2(\omega - \omega_0)^2 + \frac{1}{3!}\beta_3(\omega - \omega_0)^3 + \ldots, \tag{3}$$

and its derivative is

$$\frac{d\beta}{d\omega} = \beta_1 + \beta_2(\omega - \omega_0) + \frac{1}{2!}\beta_3(\omega - \omega_0)^2 + \ldots \ , \tag{4}$$

where the first term is constant in frequency, representing the path length difference of the interferometer arms. By fitting the acquired group delay curve to Eq. (4), the group velocity dispersion, β_2, and higher order dispersion terms are determined.

Obtaining the Group Delay from Spectral Interferogram

The interference spectrum, shown in Figure 2, has sinusoidal fringes which vary in periodicity due to the different phase delays arising from a frequency dependent refractive index. By finding the local periodicity at each point in the interferogram, the group delay of the device under test is determined[15].

Traditionally, the Fourier transform technique is used to recover the spectral phase of the signal and numerical differentiation is then required to calculate the group delay.

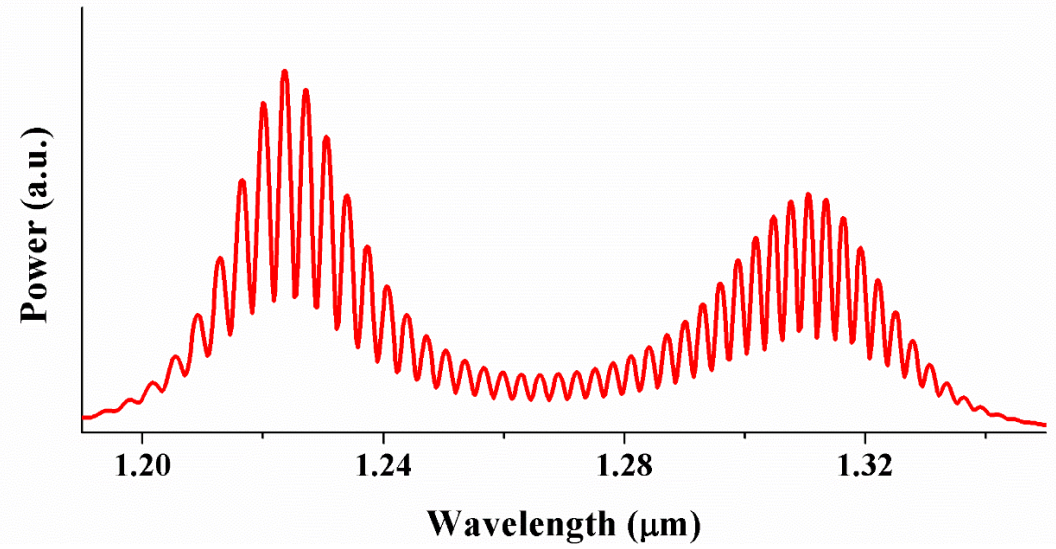

Figure 2. Spectral interferogram of a quantum dot semiconductor optical amplifier recorded on an optical spectrum analyzer. The change in periodicity of the interference fringes across the spectrum gives information on the group delay of the device under test.

This process often requires smoothing functions to reduce the amplification of noise in the data. Numerical differentiation and smoothing functions can be avoided by the use of the wavelet transform (WT). As shown by Deng et. al.[16], a WT will extract the group delay directly from the interferogram. While this method requires more processing time than the Fourier transform method, it is handled readily by current desktop computers.

To calculate the WT, the overlap integral of the interference spectrum and a user-defined wavelet function with a known periodicity is calculated. The wavelet period is varied to find the period for which the overlap integral is maximized. This is done for each measured frequency in the interferogram. The result is the local periodicity at each point in the interferogram, i.e. the group delay. Figure 3 shows the WT result, a contour plot where the maximum at each wavelength value corresponds to the group delay value for that wavelength.

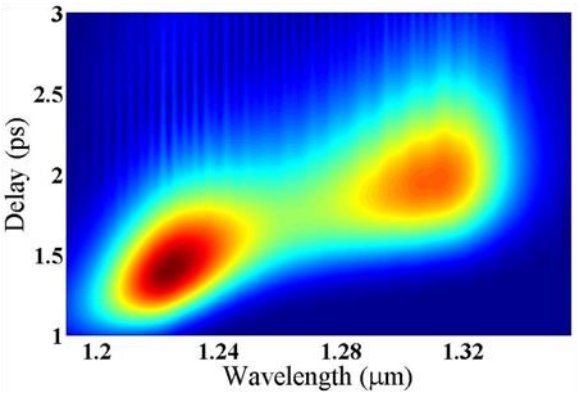

Figure 3. Contour plot of the wavelet transform of the spectral interferogram. The maximum for each wavelength is the group delay.

Group Delay Dispersion Measurement of QD SOA

Interference spectra are acquired using a Mach-Zehnder interferometer. This configuration, shown in Figure 1, is chosen for ease of alignment and to measure the group delay on a single pass through the sample. The light source is a 3 mm SOA fabricated from the same wafer as the 2 mm SOA under test.

Dispersion characteristics are measured for a 10-layer InAs/GaAs quantum dot SOA with a 4 μm wide waveguide. The uncoated facets were fabricated at a 7º angle to minimize reflections. The device is mounted p side up on a copper stud with gold coating for electrical and heat conductivity. A thermoelectric cooler and thermistor are used to for temperature stabilization.

The SOA is placed between two microscope objective collimating lenses. An identical pair of lenses is placed in the reference arm of the interferometer to compensate for the dispersion induced by the lenses. In order to observe the group delay dependence on injection current, the device is measured at injection currents ranging from 100 mA to 500 mA. Figure 4 shows the measured power spectral density at these injection current values.

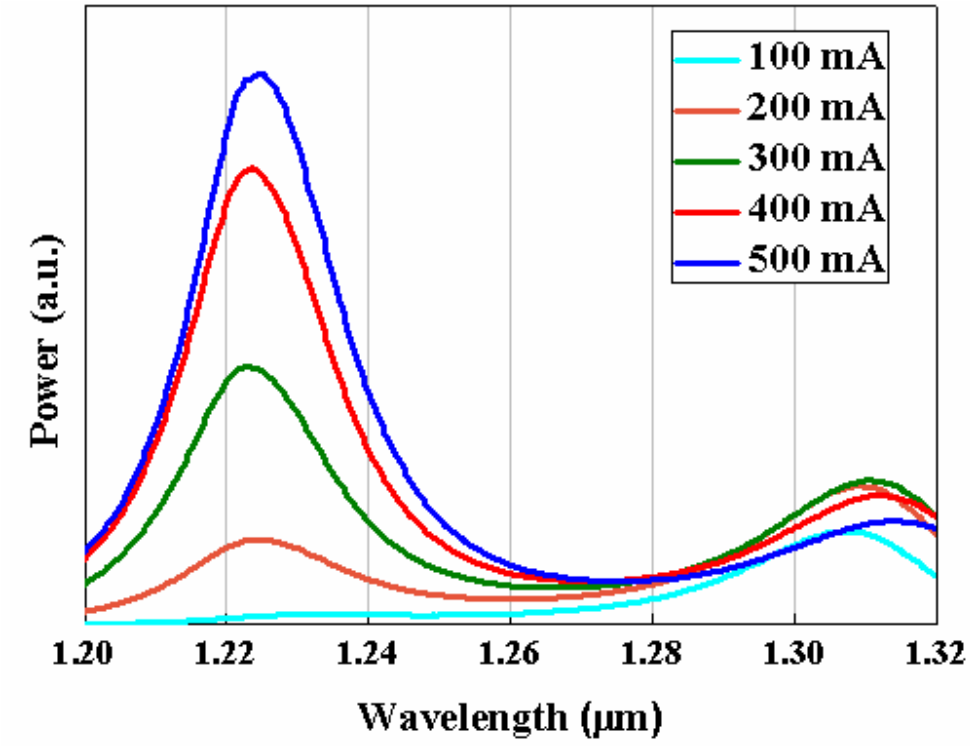

Figure 4. Quantum dot semiconductor optical amplifier dispersion measurement results at measured injection currents.

A gold rooftop mirror on a micrometer stage is placed in one interferometer arm for use as a variable optical delay to control the path length difference between the two interferometer arms.

It is necessary to first take a measurement with only the lens pairs in each arm to calculate the background group delay arising from bias in the interferometer[17]. Bias arises from optical path length mismatch caused by mirrors and lenses which are not identical, imperfections in the beam splitters and a small amount of dispersion caused by the free space path length difference. The group delay bias was found to deviate less than 10 fs from the average value in the region of interest, spanning 120 nm.

The group delay for the SOA (Figure 5) shows anomalous dispersion with 800 fs differential delay across the measured spectrum. Delay is seen to decrease with increasing injection current, though not uniformly across the spectrum. The decrease is most pronounced near the first excited state peak (1.23 μm), changing by approximately -15 fs per 100 mA. The ground state (1.31 μm) exhibits less of a dependence on injection current, changing by -15 fs over the entire 400 mA increase.

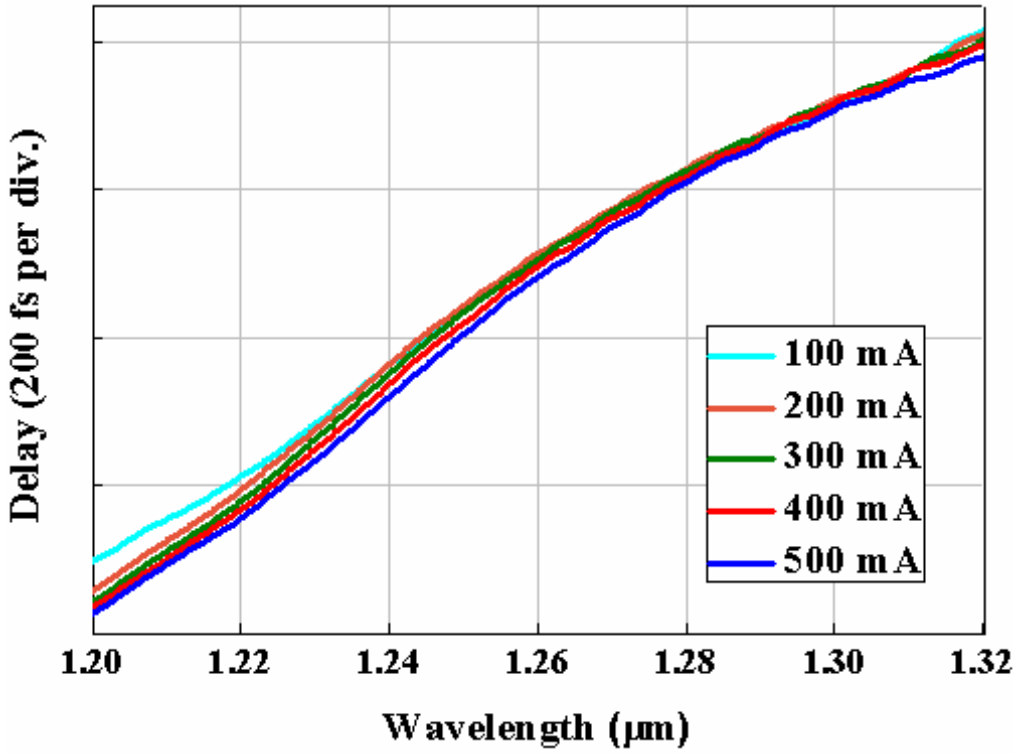

Figure 5. Group delay at measured injection currents.

The magnitude of the group velocity dispersion tends to increase with injection current. Under 100 mA of injected current, β_2 is -5.7×10^3 fs^2 (6.7 fs/nm) where, at 500 mA, it is -6.3×10^3 fs^2 (7.6 fs/nm). This amount of dispersion is of the same order of magnitude

as that of other semiconductor materials and devices[17,18], after normalizing for injection current and device length.

In addition to the large linear dispersion of the group delay, higher orders are observed. The Taylor expansion of group delay with 500 mA of injection current shows measureable quadratic, cubic, and higher order dispersion: $\beta_3 = 4.0\times10^4$ fs^3, $\beta_4 = 1.3\times10^6$ fs^4 and $\beta_5 = 4.6\times10^7$ fs^5. The cubic dispersion is evident in Figure 5 by a change in concavity, from concave up at short wavelengths, to concave down at longer ones.

Measuring the dispersion characteristics of an InAs/GaAs QD-SOA at various injection currents provides information which is useful for future generation of wide-band mode-locked laser spectra based on semiconductor devices. These results show a predominant anomalous dispersion with measurable higher order terms. The Taylor expansion coefficients for the dispersion of the device at 500 mA of injected current are $\beta_2 = -6.3\times10^3$ fs^2, $\beta_3 = 4.0\times10^4$ fs^3, $\beta_4 = 1.3\times10^6$ fs^4 and $\beta_5 = 4.6\times10^7$ fs^5. Also, while the group delay decreases with increasing injection current, the magnitude of the group velocity dispersion increases.

RF Heterodyne Interferometry

Optical spectral interferometry requires that the path length difference between the two interferometer arms be nearly equal. The interference fringes on the spectral interferogram are inversely proportional to the difference in path length, thus just 2 cm of path length difference will result in a fringe spacing of 10 GHz at which standard optical spectrum analyzers can no longer resolve the fringes. If measuring longer path length

differences is required, higher resolution can be obtained by first photo detecting and then combining the signals for analysis on an RF spectrum analyzer.

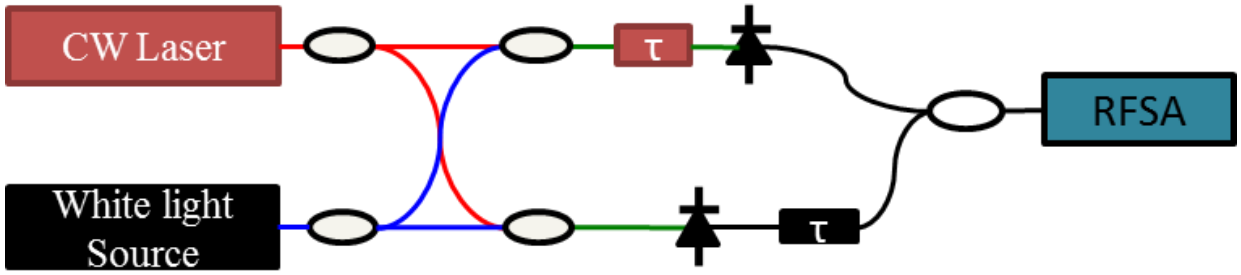

Figure 6 Setup for RF heterodyne interferometry. The narrow band white light source is split and combined with the cw laser for heterodyne detection. The resulting electrical signals are combined and observed on an RF spectrum analyzer.

Figure 6 shows the setup for heterodyne interferometry. A narrow band, white light source is split and combined with a CW laser as a local oscillator before photodetection. The resulting electrical signals are combined and observed on an RF spectrum analyzer (RFSA).

Figure 7 shows RFSA traces resulting from optical delays of 24 cm (a), and 56 cm (b). With fringe spacings of 833 MHz and 353 MHz, respectively, they would not be resolvable on optical equipment but are easily resolved with the high resolution of the RFSA.

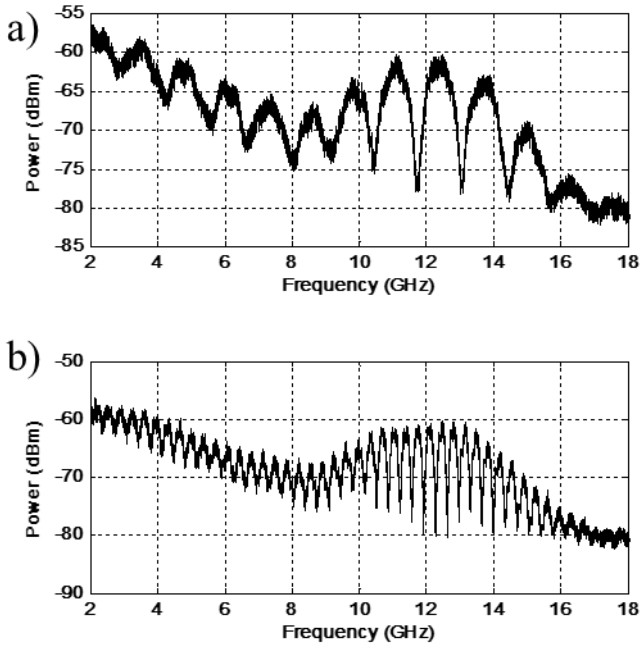

Figure 7. Heterodyne interferograms at delays of 24 cm (a) and 56 cm (b).

By combining elements from both optical spectral interferometry and RF heterodyne interferometry, advantages from both can lead to high resolution delay measurement at long delays. Multi-heterodyne techniques allow information from large optical spectra to be processed on low bandwidth, high resolution electronic equipment. As well, once downconverted, the signals can be sampled and recorded for offline analysis.

Multi-Heterodyne Detection and Sampling

Multi-Heterodyne Introduction

Multi-heterodyne (MH) measurements take advantage of the narrow linewidth and frequency stability of the individual comb lines of optical frequency combs to sample

periodic optical signals by down-converting them to the RF domain. Several measurement applications take advantage of the technique to characterize a variety of optical signals.

By using a pair of mutually coherent frequency combs, one comb can be used as a reference while the other is passed through a sample under test. This technique has been used to obtain the full complex response of gas samples across large spectral bandwidths[19,20,21] and absolute distance measurements across many kilometers[22,23] by combining time-of-flight measurements of the optical pulses with phase sensitive detection. Additionally, periodic optical signals themselves may be characterized in amplitude and phase with high resolution[24,25,26]. These measurements benefit from the mutual coherence between the sources, allowing acquisition times to be extended beyond the coherence time of either source to greatly increase the signal-to-noise ratio.

As well, MH techniques may be used to spectrally compress and down-convert periodic optical waveforms which are not coherent with the local oscillator[30]. For a source with sufficiently narrow linewidth and frequency stable comb-lines, MH measurements can be performed with acquisition times on the order of the coherence time of the source. For even moderately stable combs, coherence times can be on the order of microseconds, allowing for long enough acquisition times to achieve acceptable signal-to-noise for many applications. This technique has been shown to reliably record the amplitude and phase information from two mutually incoherent comb sources, CW laser light that has been phase modulated, and even broadband, incoherent light which has been periodically filtered.

Multi-Heterodyne Detection with White Light

This work describes experiments made by performing MH detection to downconvert periodically filtered white light[27]. The ability to compress and down-convert large spectral bandwidths to the RF band allows accurate sampling and recording of the amplitude and phase of the filtered white light. This ability becomes useful when comparing delays between two independently detected signals which originated from a single source. Though the white light is a signal with randomly-varying phase, two independently photodetected signals originating from the same source continue to show correlation[28]. By electronically sampling the two signals, the time delay can be determined with a simple cross-correlation. The result of the cross-correlation is a sharp peak at the time delay between the sampling time of each signal.

A traditional heterodyne approach to this method of delay measurement has a resolution determined by the inverse of the RF bandwidth of the sampling electronics. Thus, an oscilloscope with 10 GHz of bandwidth can determine time delays to within 1 ns, or 30 mm of distance in free space.

Periodic filtering along with multi-heterodyne detection and sampling of the signal records data from a much broader optical bandwidth making the new limit of the resolution that of the optical bandwidth of the narrower of the signal source or reference comb.

A frequency domain explanation of the process is shown in Figure 8. In the optical frequency domain, each etalon passband has a closely neighboring local oscillator with each passband/oscillator pair at different frequency offsets than each other pair within the detection bandwidth. Upon photodetection, an RF spectrum trace shows that each heterodyne pair maps to a different frequency bin in the RF domain with the phase and

amplitude preserved. In this way, data that is widely spaced in the optical domain is compressed to a narrower RF bandwidth.

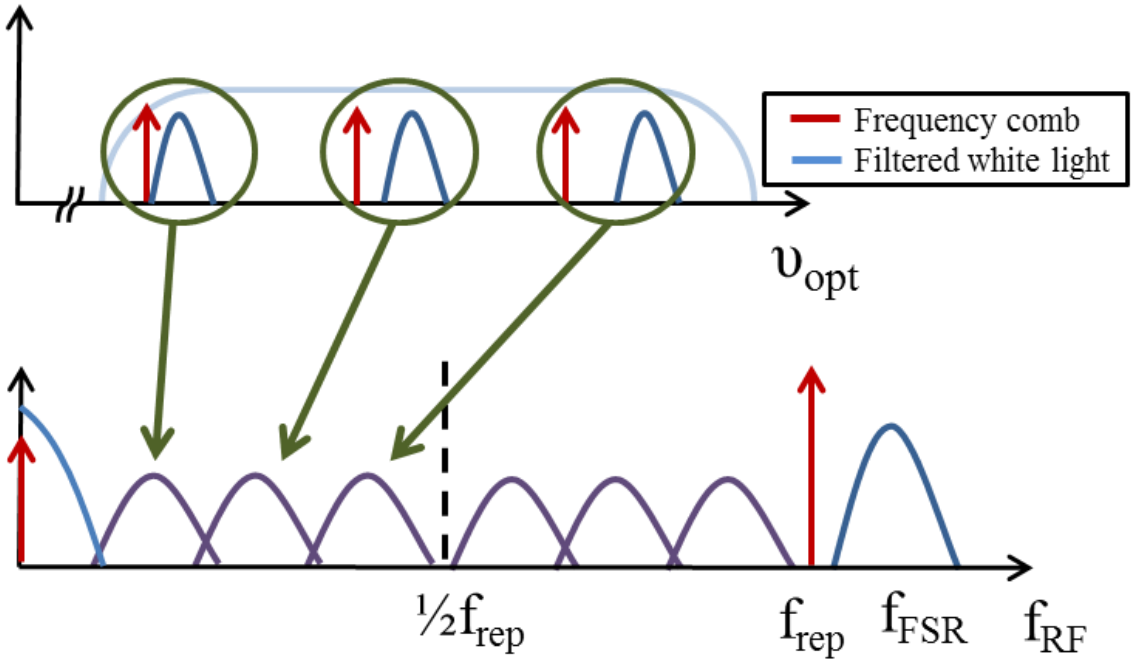

Figure 8. Multiheterodyne detection in the frequency domain.

In the time domain description (Figure 9), light enters the etalon as random noise. Upon each successive round trip, a small portion of the light is transmitted and much of it is reflected, causing the light exiting the etalon to be largely correlated with the light at multiples of the round trip distance of the etalon for a time corresponding to the ring down time of the etalon. The period of the MLL is chosen to be slightly offset from the etalon round trip time. As each laser pulse arrives at the photodetector, it beats with a different portion of the pseudo-periodic waveform. After a time determined by the offset between the etalon round trip time and the laser repetition rate, the pulses retrace

the waveform, which is still highly correlated with its previous iteration due to the etalon's relatively high finesse.

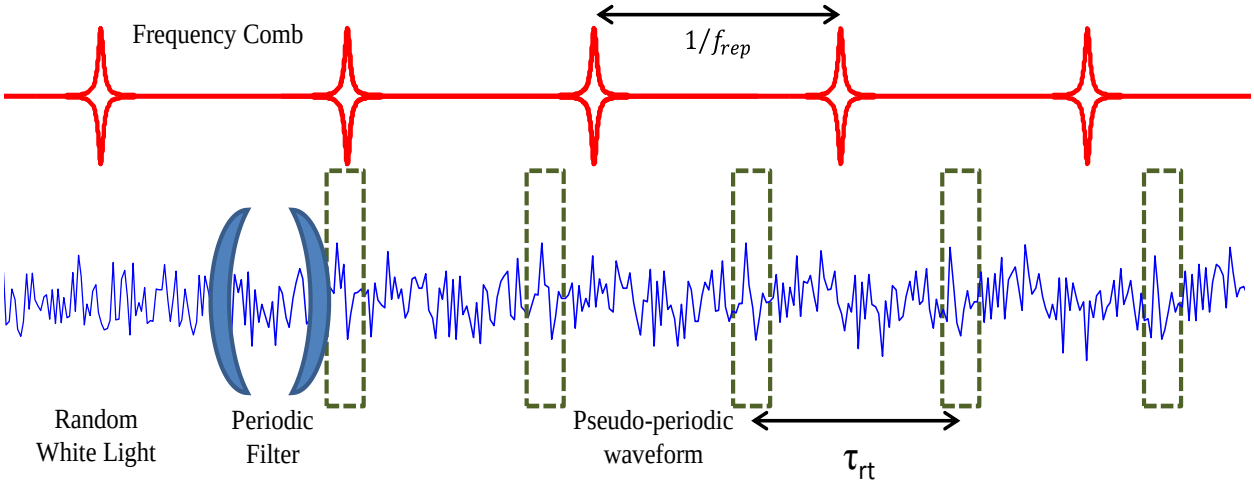

Figure 9. Multiheterodyne detection in the time domain

Theory and Simulation

By introducing a frequency detuning, δ_{det}, between the etalon FSR and laser repetition rate defined to be

$$\delta_{det} = | f_{fsr} - f_{rep} |, \quad (5)$$

upon photodetection, each etalon filtered peak in the optical frequency domain is down-converted to a different portion of RF spectrum while preserving both the amplitude and phase of each filtered passband (Figure 8). Using the frequency comb as a reference, the white light peaks are mapped into the RF domain at specific frequency intervals given by the detuning frequency. This mapping can be described as a compression factor, which is the ratio between the etalon FSR and the detuning frequency:

$$C \equiv \frac{f_{fsr}}{\delta_{\text{det}}} \tag{6}$$

For the phase of each filtered white light peak to be preserved, the detuning frequency must be greater than the width of an etalon resonance, such that neighboring peaks in the RF domain do not overlap. By setting the minimum detuning frequency to be the full width at half maximum (FWHM) of an etalon resonance, we can see that there is a maximum compression factor for a given etalon:

$$C_{\max} \equiv \frac{f_{fsr}}{FWHM} \ , \tag{7}$$

which is simply the definition of the etalon finesse.

The compression factor may be understood in the time domain by considering that the periodic filtering of the etalon imposes correlations on the white light signal at intervals of the round trip time of the etalon (Figure 9). When the periodically correlated signal is combined with the comb source, the mismatched periods cause a slippage of successive laser pulses along the white light such that correlations of the total signal occur at intervals given by the inverse of the frequency detuning. Thus, a measured shift along the time axis in a multiheterodyne correlation signal corresponds to real time delays which are shorter by a factor of *C*. By accurately measuring the etalon FSR[29] and with precise control of the laser repetition rate, the compression factor may be determined to an accuracy of as high as 10 parts per billion.

To develop an analytical expression for a multi-heterodyne cross-correlation of a frequency comb with periodically filtered white light, we start with a single heterodyne of a local oscillator with a band-limited, incoherent source.

The total electric field at the detector for a heterodyne measurement of a single local oscillator with a band-limited, incoherent source is given by:

$$E_{tot}(t) = 2A\cos(2\pi\upsilon_L t + \phi_L) + 2\sum_{n=n_0}^{n_0+N} |q_n| \cos\left(\frac{2\pi n}{\tau} t + \phi_n\right) \tag{8}$$

where the first term represents the local oscillator, which is assumed to be a delta function at frequency v_L with phase φ_L, and the second term is a Fourier representation of band-limited incoherent light[30] where τ is the total acquisition time of the measurement and q_n and φ_n represent the amplitude and a random phase, respectively, of the nth frequency component. The photodetected signal contains a constant DC signal from the laser source and each amplified spontaneous emission (ASE) component's self-beating, homodyne components from ASE-ASE beats, and the signal of interest, the heterodyne component, which is easily high pass filtered. A step-by-step computation of the cross correlation of a heterodyne signal with an identical delayed signal is left to an appendix. The resulting expression is:

$$S_{1,2}(t) = 4\Re^2 R_L^2 P_L \sum_n P_n \cos\left[2\pi\left(\frac{n}{\tau} - \upsilon_L\right)\left(t + \Delta T + \Delta t_{ase}\right) + 2\pi\upsilon_L\left(\Delta t_{ase} - \Delta t_L\right)\right], \tag{9}$$

where $\Re$ is the responsivity of the photodetector, R_L represents the photodetector load resistor, P_L is the laser power, and P_n describes the spectral envelope of the white light, in our case, given by the etalon transfer function. The delays, Δt_{ase} and Δt_L, shown in Figure 1, are the unique delays experienced after each source is split and before they are combined with a fiber coupler. ΔT is the delay that is common to both the ASE and laser sources after combining. We can see in a simulation that the resulting correlation resembles a pulse in time (Fig. 3(a)) with an envelope determined by the Fourier

transform of an etalon passband, centered at the offset ($\Delta T+\Delta t_{ase}$),the total ASE path delay. It has a “carrier frequency” given by the average of (n/τ-ν_L) weighted by P_n, the frequency difference between the optical comb line and the Fourier component of white light. The second term of the cosine function is a phase offset which is proportional to the comb line frequency and the difference in the laser and ASE delays.

A multi-heterodyne cross-correlation may be taken as a superposition of several heterodyne signals on the condition that the beat products do not overlap in the RF domain. This ensures that the phase of each heterodyne signal is preserved. For experimental distance measurements, Δt_L should be well stabilized. For brevity here, Δt_L is assumed to be zero, though it is carried through in the appendix calculations. The analytic expression for a multi-heterodyne cross-correlation made up of *m* beat products is then given by:

$$S_{1,2}(t) = 4\Re^2 R_L^2 P_L \left[\frac{\sin(m\alpha)}{\sin(\alpha)}\right]\sum_n P_n \cos(\varphi) \tag{10}$$

with

$$\varphi = 2\pi\left(\frac{n}{\tau} - \upsilon_L + (m-1)\frac{\delta_{\text{det}}}{2}\right)\left(t + \Delta T + \Delta t_{ase}\right) + 2\pi\left(\upsilon_L + (m-1)\frac{f_{rep}}{2}\right)\Delta t_{ase} \tag{11}$$

and

$$\alpha = \pi\delta_{\text{det}}\left(t + \Delta T\right) + \pi f_{fsr}\Delta t_{ase} \tag{12}$$

where f_{rep} is the laser repetition rate, and f_{fsr} is the etalon free spectral range and δ_{det} is the detuning frequency.

The cosine term in Eqn. (5) is similar to that of Eqn. (4) with a slightly modified carrier and offset phase term and the envelope still centered at the total delay between the two signal paths. The term in brackets in Eqn. (6) describes the multiple interference present in the cross-correlation of a set of *m* non-overlapping heterodyne beats. We can see from the α term that features are spaced at multiples of $1/\delta_{det}$ and undergo a full π phase shift for a delay change, Δt_{ase} of $1/f_{fsr}$ or τ_{rt}. This is the mathematical manifestation of the compression factor. Figure 10 shows simulation results of a single heterodyne cross-correlation, as well as multiheterodyne cross correlation simulations with three and ten beat products. Analogous to a multiple slit interference experiment, we can see that addition of heterodyne beat products contributes to a narrowing of the features in the cross-correlation.

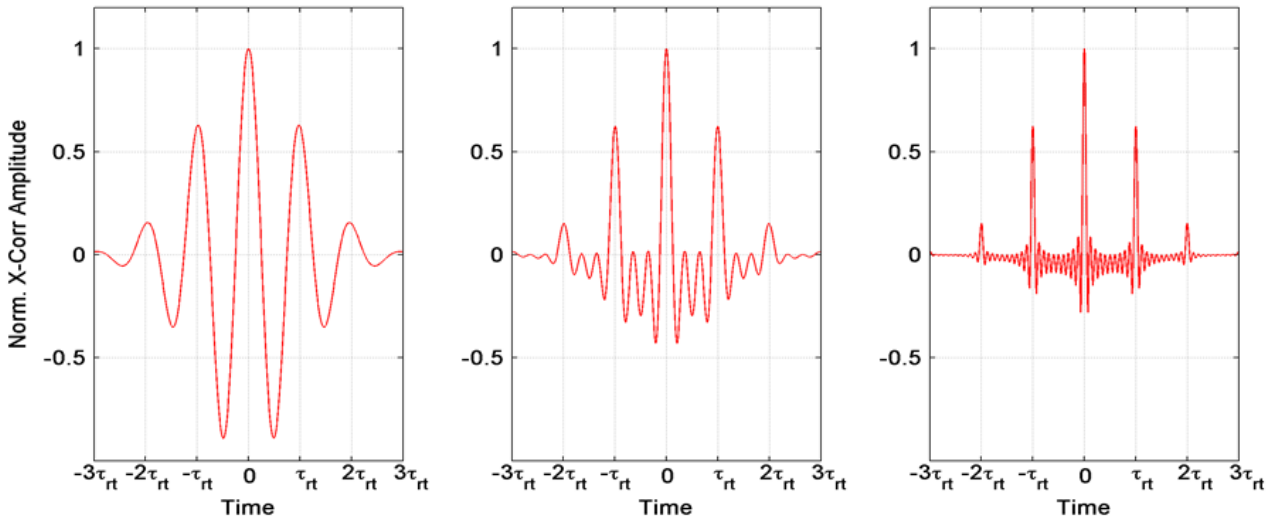

Figure 10. Simulation result for cross-correlation of (left) a single heterodyne measurement, (middle) a multiheterodyne with three etalon passbands, and (right) ten etalon passbands. The time axis has been shifted to emphasize the structure of the cross-correlations, with features spaced at τ_{rt}.

Experiment

A schematic of the experimental setup is shown in Figure 11. Incoherent white light, filtered by a Fabry-Perot etalon is split and a delay introduced between the two paths. Each is combined with the mode-locked laser whose repetition rate is detuned from the etalon free spectral range (FSR). The resulting signals are photodetected and sampled on a high speed oscilloscope. Cross-correlations of the MH signals show correlations present with high signal-to-noise at delays of up to 20 km. The maximum delay range is limited by the 500 μs capture time of the high speed oscilloscope and delay changes of less than a millimeter are clearly resolved.

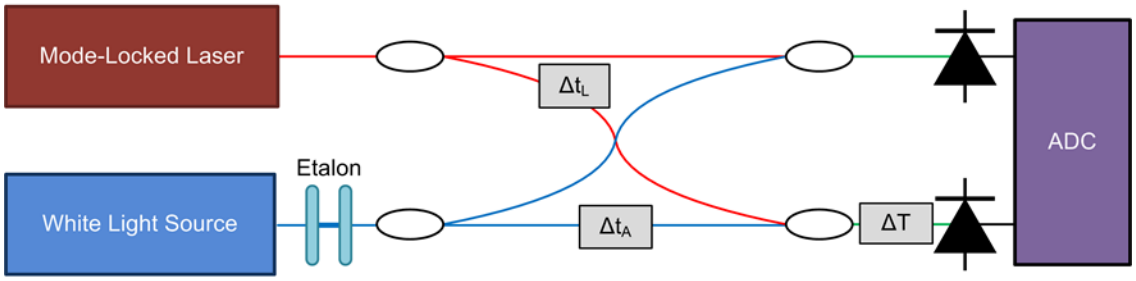

Figure 11. Setup for sampling periodically filtered white light. Δt_A is the optical delay difference between the paths, Δt_L is the delay between the laser paths, ΔT is the delay difference between the RF paths, the ADC is the analog-to-digital converter that samples the RF signal.

The white light source used in this experiment is ASE from a semiconductor optical amplifier. The signal is amplified and then passed through the Fabry-Perot etalon, which has an FSR of 10.24 GHz and a finesse of ~100, giving passbands of 100 MHz FWHM. A schematic of the white light source configuration is showing in Figure 12.

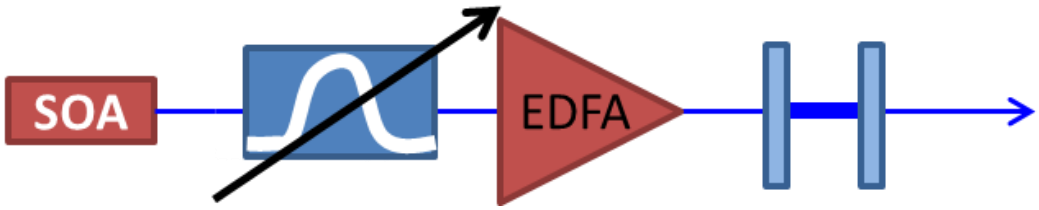

Figure 12. White light source. A free-running semiconductor optical amplifier output is filtered with a 100 nm bandpass filter. The output is amplified with an Erbium-Doped Fiber Amplifier (EDFA) and then filtered with the Fabry-Perot etalon.

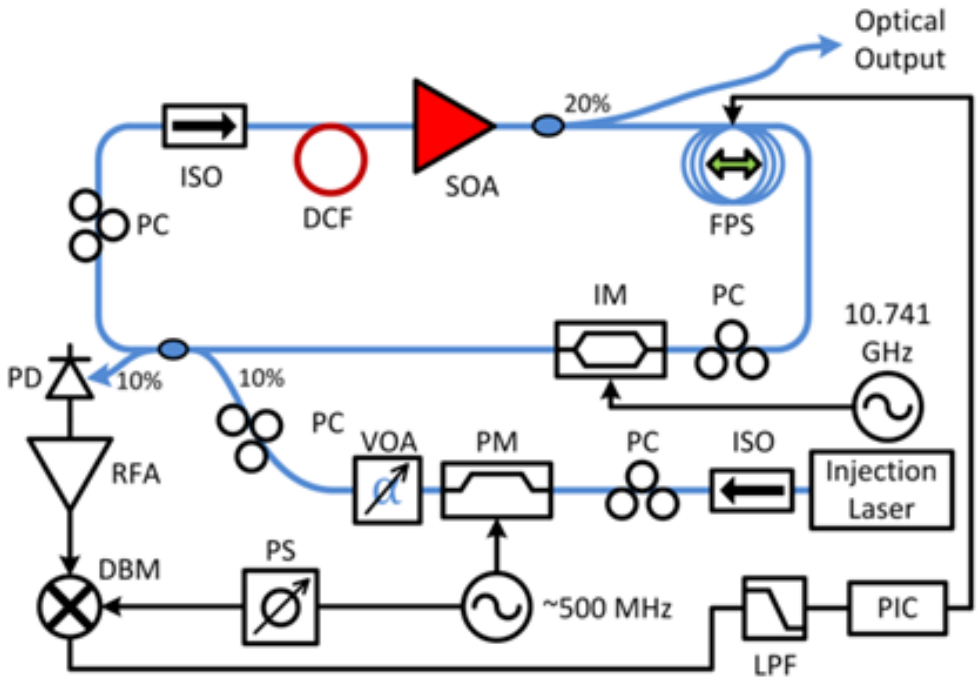

Figure 13. Frequency comb source schematic with optical path (blue) and RF path (black). SOA, semiconductor optical amplifier; FPS, fiber phase shifter; PC, polarization controller; IM, intensity modulator; ISO, optical isolator; DCF, dispersion compensating fiber; PD, photodiode; RFA, RF amplifier; DBM, double-balanced mixer; PS, phase shifter; LPF, low pass filter; PIC, proportional integral controller

The frequency comb source is a semiconductor-based, actively mode-locked, injection-locked, stabilized laser. Figure 13. Shows the schematic of the laser setup. An

intensity modulator acts as the active mode-locking mechanism and can be easily tuned by changing the synthesizer's driving frequency.

The operating frequency is 10.74 GHz, chosen to have a 500 MHz detuning from the etalon FSR to ensure that there is no overlap of the multi-heterodyne beat tones in the RF domain. Because the fundamental frequency of the laser cavity is ~40 MHz, injection locking with a narrow linewidth, CW laser source is required to select a single supermode set and suppress all spurious supermode sets. As a result of the injection locking, a stable 10.74 GHz comb spectrum is created with individual comb-lines exhibiting a linewidth of ~1 kHz, which is that of the CW source. The narrow linewidth of the comb source ensures that the heterodyne beat tones in the RF domain are accurate representations optical signals. The overlaid optical spectra of the sources are shown in Figure 14.

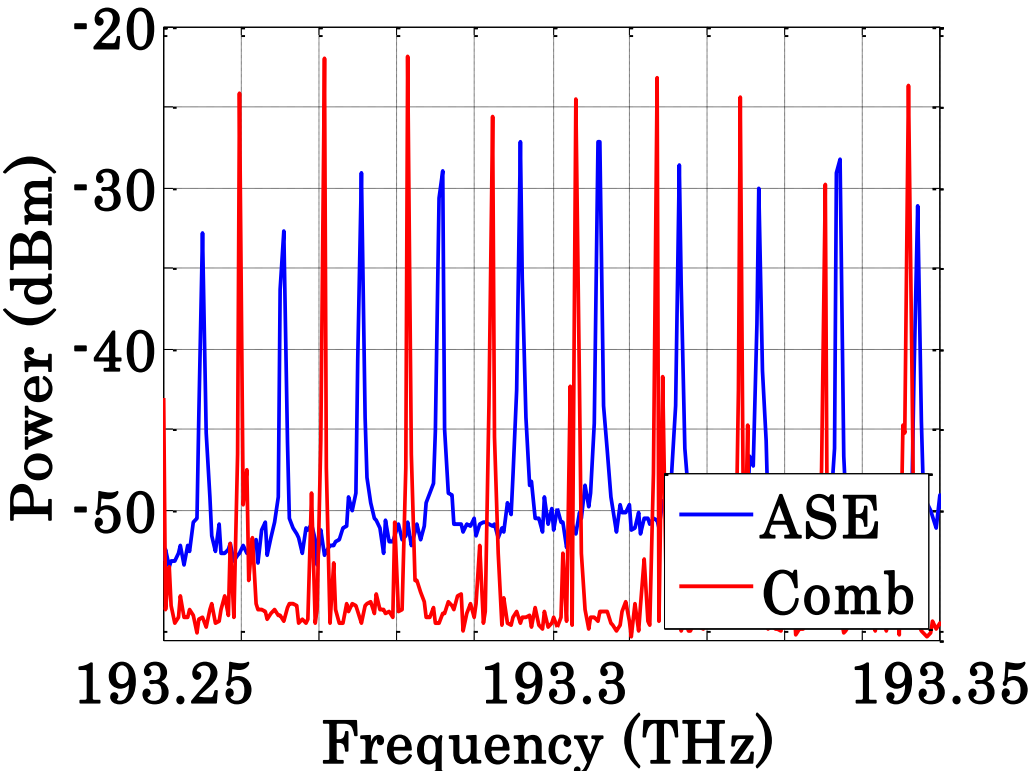

Figure 14. Overlaid optical spectra of etalon filtered ASE (blue) and MLL comb source (red).

The white light signal is split and a delay introduced before combining with the comb source and photodetecting. After photodetection, the signals are sampled on a high speed oscilloscope. Correlation between the detected signals for a short, 2.8 ns delay is visible in the time domain waveforms (Figure 15(a)). The RF spectrum of a single channel shows the compression of the white light peaks, spaced at 10.24 GHz in the optical domain, spaced at the detuning frequency of 500 MHz (Figure 15(b)). The large signal near DC is a result of the superposition of the direct detection of all of the etalon filtered peaks and may be filtered out digitally in post processing to view only multiheterodyne cross correlations.

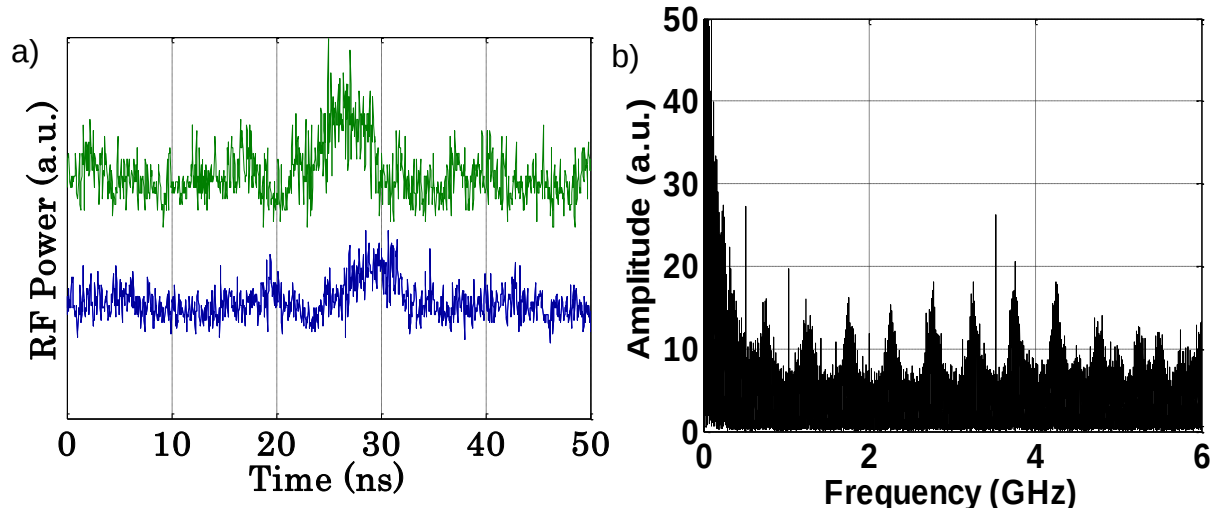

Figure 15. a) Sampled waveforms with a delay of 2.8 ns b) RF spectrum of a single channel multiheterodyne measurement showing 500 MHz detuning frequency. Sharp features near 400 MHz, 1 GHz, and 3.75 GHz are artifacts from the mode-locked laser source.

The voltages across the photodetector load resistors are sampled at 25 Gsamples/sec and stored for offline analysis. Figure 7 a) shows the recorded time domain signals from each detector with a 2.8 ns delay present between the two detected signals. Figure 7 b) shows the RF spectrum of the Fourier transformed signal. The RF spectrum shows a large signal near DC, which is the homodyne beating between frequencies within each individual etalon passband. Peaks spaced by 500 MHz are clearly visible as the multi-heterodyne signal of interest. As well, several peaks occurring at 400 MHz, 1 GHz, and 3.75 GHz are artifacts present in the mode-locked laser source.

Cross-correlations of two cases are shown in Figure 16. A short delay as well as a delay with a ~13.5 m section of SMF added are shown. The figures show peaks with

>18dBm SNR, centered at the time delay between the two signals as well as smaller features, which correspond the multi-heterodyne portion of the signal.

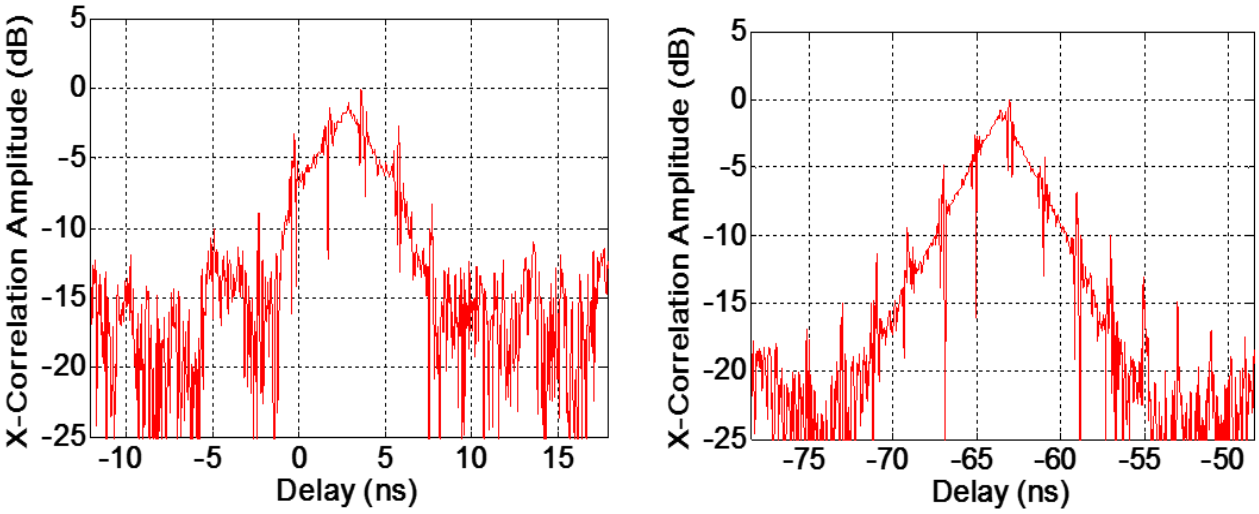

Figure 16. Multi-heterodyne cross-correlations with a short delay and with 13 m of SMF added. The signal shows high SNR with good resolution of MH features.

Figure 16 b shows a shift of 66.5 ns, corresponding to the optical path length difference between the two cases (13.6 m assuming $n_{SMF} = 1.468$).

It is useful to separate the homodyne and MH components to discuss the information they each contain and the origin of their characteristics. This is easily done by digitally filtering before cross-correlation, using low pass filtering and high pass filtering for the respective homodyne and MH signals. Figure 17 shows the filtered cross-correlations on a linear scale.

The homodyne plot (Figure 17(a)) is centered at time delay between the two signals. As mentioned previously, this portion of the cross-correlation comes from the superposition of the beating of frequencies within each individual Fabry-Perot etalon

passband. Thus, its resolution is limited by the 100 MHz FWHM of the etalon and provides timing resolution on the order of 10 ns.

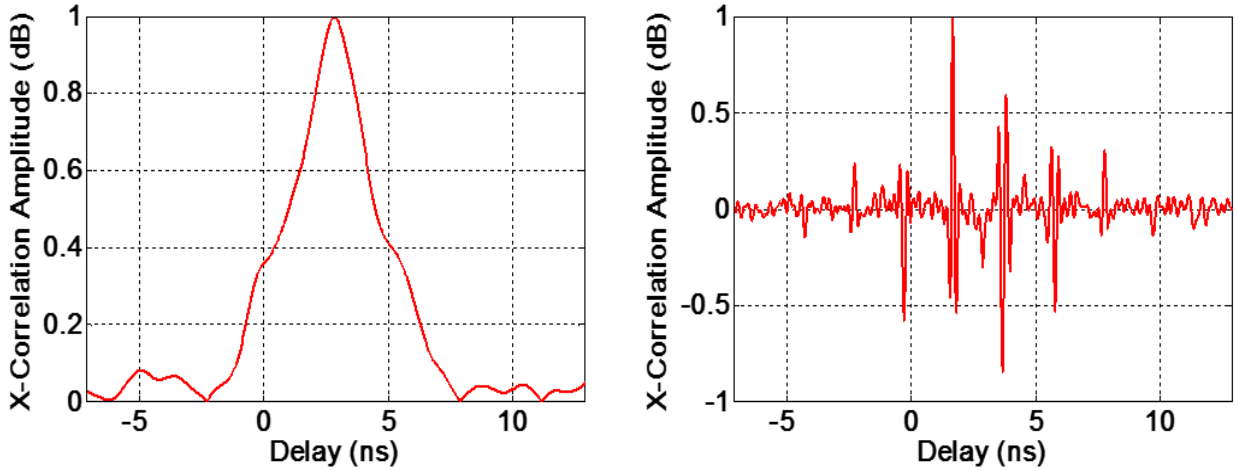

Figure 17. Digitally filtered homodyne (a) and multi-heterodyne (b) signals taken from Figure 16(a). The homodyne plot provides a low resolution estimate of the optical delay between signals. The MH plot shows small difference in delay.

The MH plot (Figure 17(b)) is a result of the superposition of the heterodyne beats between each Fabry-Perot passband and a laser comb-line. It contains features with a separation of 2 ns, corresponding to the inverse of the detuning frequency of 500 MHz. However, because of the precise mapping of the 500 MHz separation of peaks in the RF spectrum to the 10.24 GHz separation of the etalon passbands, shifts of these features correspond to changes in the time delay between signals which are shorter by a factor of 20.48, the compression factor. Thus for the 40 ps sampling period of the oscilloscope, a shift of a cross-correlation feature on the time axis of a single point corresponds to a 1.95 ps delay change of the optical signals, or 590 μm distance in free space.

Cross-correlations of the digitized signals with 20 km (20,019 ± 0.5 m) of dispersion shifted fiber delay and 20 km with 115 cm of standard single mode fiber added are shown in Figure 18. The correlations show greater than 22 dB SNR with 500 µs of captured data. Additionally, correlations rise to 1 dB above the noise floor with just 2 µs of correlated data.

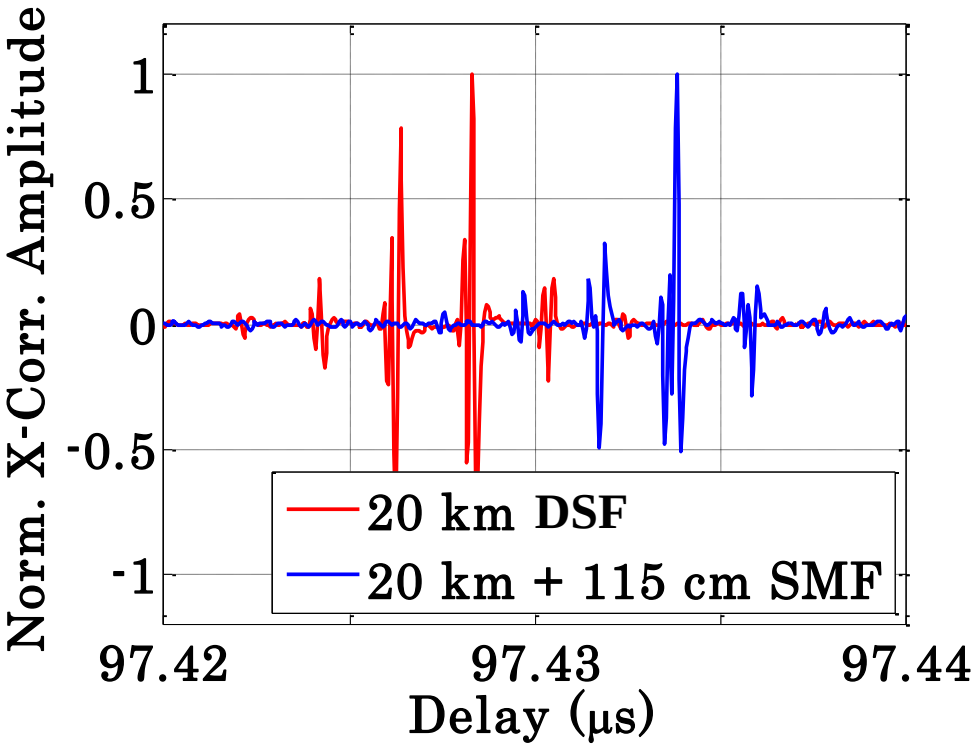

Figure 18. Multiheterodyne cross-correlations with delays of 20 km (red) of dispersion shifted fiber and at 20 km of fiber with 115 cm added (blue).

A short, free-space delay was used to show the resolution capability of the technique and avoid fiber length fluctuations. Cross-correlation measurements were performed with increasing delays in 1 mm increments. The centroid of a single multi-heterodyne cross-correlation peak was tracked. The result, shown in red in Figure

19, shows agreement with the calculated light travel time for the corresponding delay change, shown in black.

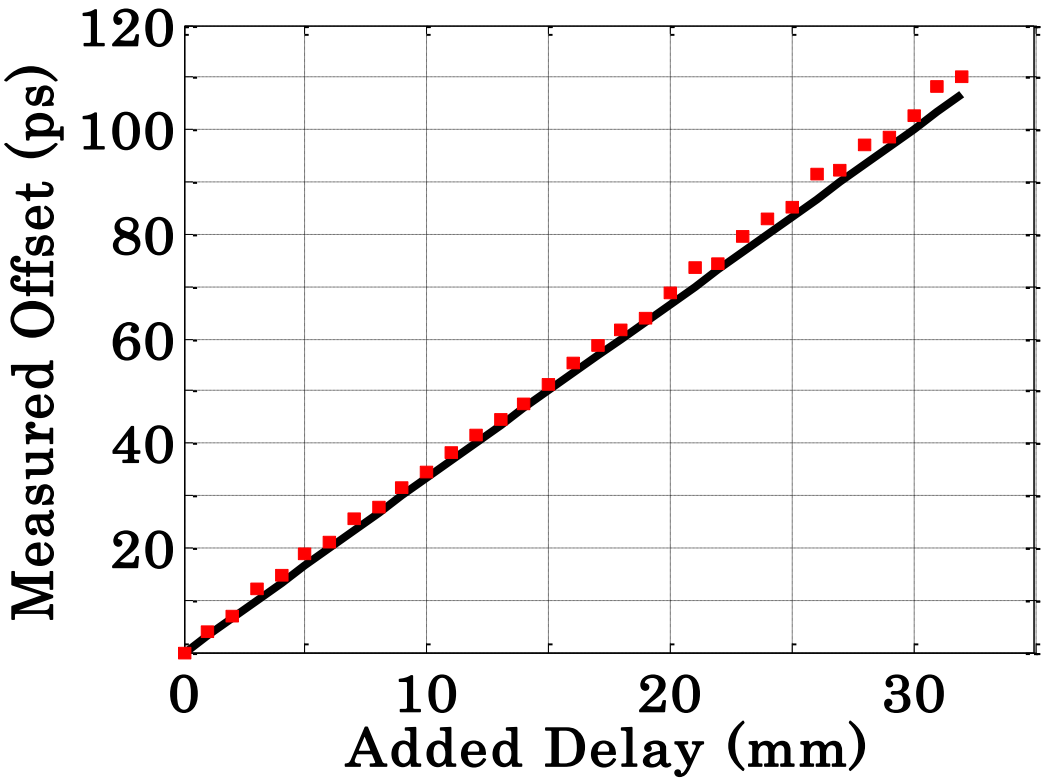

Figure 19. Plotted centroid position of correlation peak (red) measured at 1 mm intervals, using the compression factor for scaling along with the expected light travel time for light travelling in air.

CHAPTER 3: OPTOELECTRONIC OSCILLATOR

OEO Introduction

The optoelectronic oscillator (OEO) is a well-established system for producing low noise microwave tones for applications in signal processing, communications, and metrology[32]. A simple OEO loop (Figure 20) consists of a laser, optical modulator, fiber delay, photodiode, electronic filter, and RF amplifier. Modulation starts from noise in the RF amplifier and feedback over multiple round trips starts oscillation at a multiple of the fundamental frequency, determined from the gain bandwidth and modulator bias point. The OEO may have electrical output at the microwave oscillation frequency as well as optical output as modulated sidebands on the optical carrier.

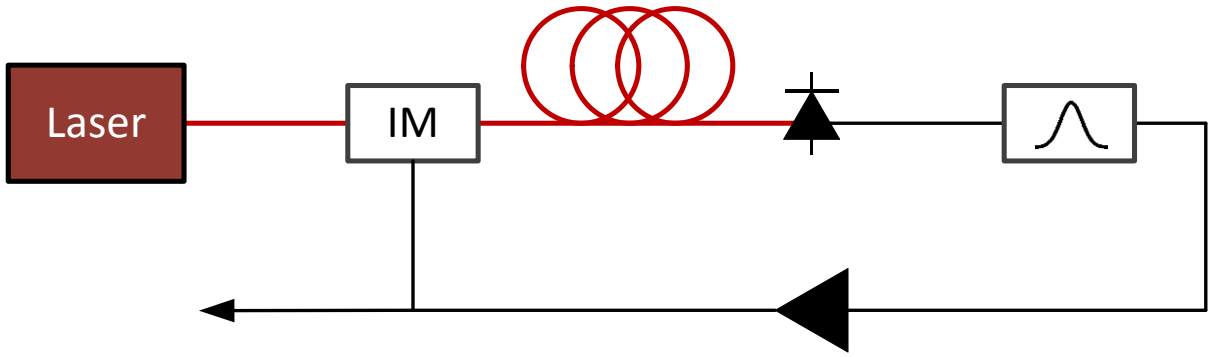

Figure 20. Basic optoelectronic oscillator. Oscillation starts from noise in the RF amplifier. Intensity modulator (IM) imparts signal on the laser before passing through a long fiber delay and photodetection. The signal is filtered with an RF bandpass filter and amplified.

The OEO is able to produce stable, low phase noise signals by taking advantage of the high quality factors made available by photonic components. The quality factor, *Q*,

of a resonator is a figure of merit describing power dissipation in a resonator and characterizes the bandwidth of the resonator with respect to its operating frequency.

$$Q = 2\pi f_0 \frac{\mathcal{E}}{P_L} = \frac{f_0}{\Delta f}, \quad (13)$$

where f_0 is the oscillator's operating frequency, $\mathcal{E}$ the energy stored, P_L the power loss, and Δf, the bandwidth of the generated tone. Standard single mode optical fiber offers the capability of extremely large energy storage with very low loss. Such low loss makes it possible to add many kilometers of optical fiber to further increase the resonator quality factor. However, as the loop length increases, the fundamental frequency of the oscillator decreases according to the equation

$$f_f = 2\pi c\tau_d, \quad (14)$$

where c is the speed of light in vacuum, and τ_d is the time delay of the loop. Thus longer delays allow for the possibility of multiple resonant frequencies within the oscillator gain bandwidth. These spurious modes compete for gain and appear as narrow peaks at multiples of the fundamental frequency in the phase noise spectrum.

With the goal of increasing loop lengths while maintaining suppression of spurious modes, filtering techniques with narrower selectivity than simple RF filters have been investigated such as multiloop operation[33,34], injection locking[35], and photonic filtering[36].

Multiloop Operation

One of the first methods of filtering spurious modes to be demonstrated, beyond placing an RF filter in the loop, was to split the signal, add different lengths of optical fiber, and recombine all within the oscillator. Loop lengths are chosen such that the desired

oscillation frequency is a common harmonic of the fundamental frequency of each loop. A dual loop oscillator will typically have a very long loop and a short loop. The long loop will provide a high quality factor for the cavity while the shorter loop provides filtering of the spurious modes, which are non-resonant within the shorter loop.

Figure 24 shows two implementations of a multi-loop OEO setup. In Figure 21(a), the output from the modulator is split into two fiber delays. Figure 21(b) shows a similar setup using a polarization beam splitter and combiner to interfere the signals in the optical domain on the photodiode[37]. In both implementations, the long loop is used as the storage element and provides a high quality factor for the oscillator. As discussed above, by itself it produces many narrow linewidth, closely spaced modes. The short loop has little effect on the quality factor of the oscillator but the relatively high fundamental frequency suppresses the non-resonant spurious modes.

Many experiments with dual loop OEOs use loops with several km of fiber delay added. These loop lengths should be locked to avoid large frequency fluctuations during long term operation.

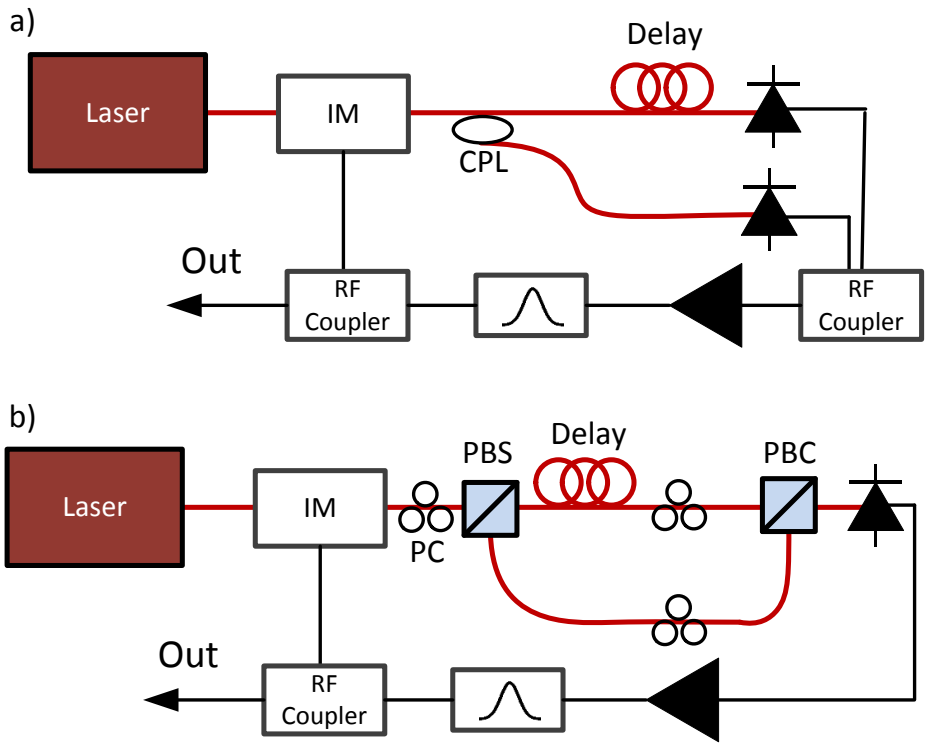

Figure 21. Examples of multiloop OEOs. a) Optical signal is split after the intensity modulator (IM), photodetected, and the photocurrents are interfered in the RF coupler. b) The optical signal is split by a polarization beam splitter (PBS) after the IM. After delays, the signal is recombined using a polarization beam combiner (PBC) and interfered on a photodiode.

Photonic Filtering

A photonic filter such as a high-Q optical cavity, whispering gallery mode resonator[38], or atomic cell may be used in addition to the RF filter in the OEO loop[36]. These filters have been shown to improve OEO stability. Unlike electronic filters, in which the bandwidth is a fraction of the center frequency, photonic filters provide passbands that are independent of microwave carrier frequency. Previous work with Fabry-Perot etalons as photonic filters in OEO systems has been performed by Cho et al.[39] and Ozdur et al.[40]. Cho et al. showed a 3.6 GHz OEO based on an etalon with 540 kHz filter

bandwidth. Both the optical frequency as well as the OEO fiber loop length were locked to the etalon to achieve long term frequency stability with an Allan deviation of 6×10^{-8}. Ozdur et al. showed work based on a 10 GHz free spectral range (FSR) etalon with a 10 MHz filter window. Phase noise of the microwave tone at 10 kHz offset was -100 dBc/Hz and showed improved frequency stability over a similar system based on an RF filter.

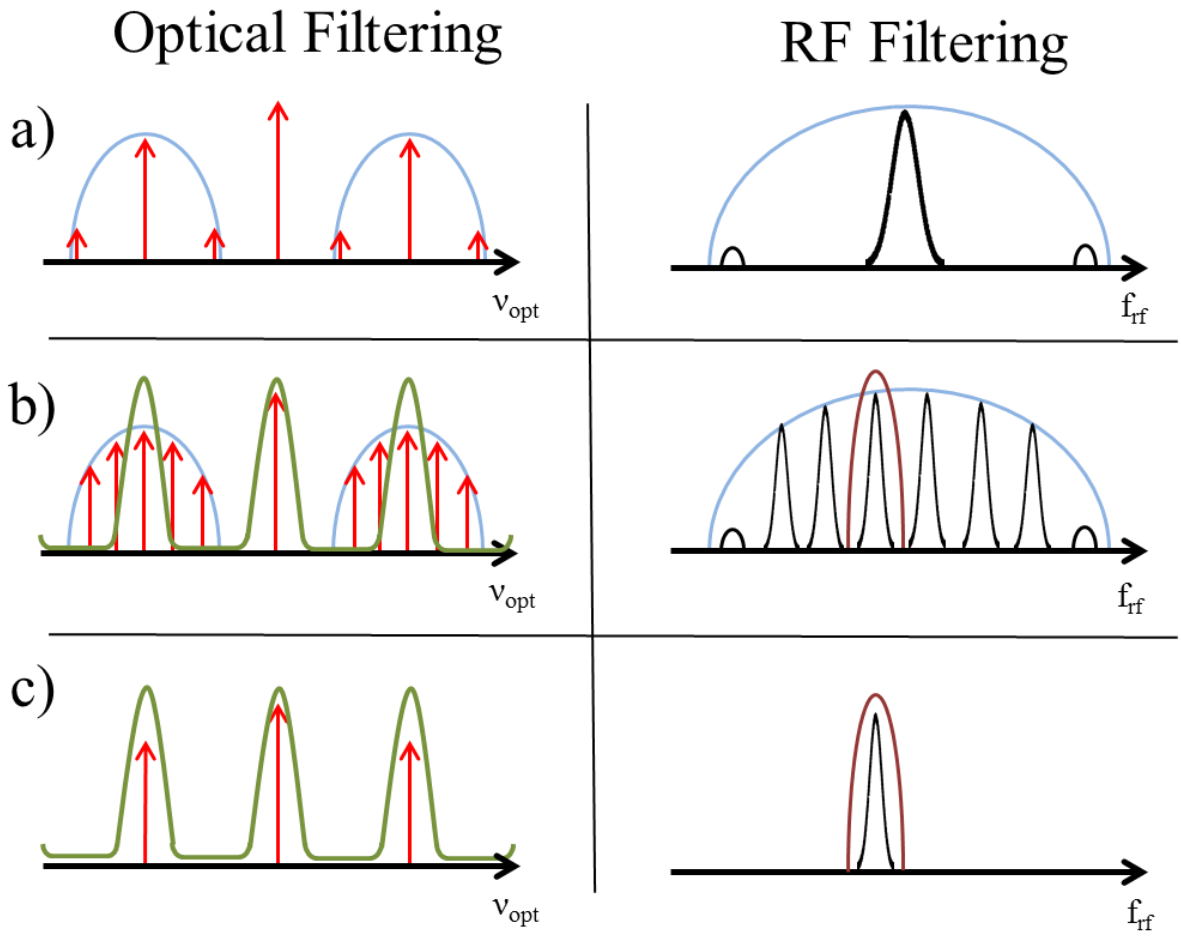

Figure 22. Comparison of filtering of spurious modes in the optical and RF domain. a) An OEO with a short loop length has widely spaced modes. Gain competition easily selects a single mode for oscillation. b) As the loop length is increased with the goal of lower phase noise, the mode spacing decreases and many modes are within the gain bandwidth. A filter is necessary to ensure single mode operation. c) Filtering in the optical or RF domain produce similar oscillating tones within the OEO.

Setup

The OEO studied in this work[41], shown in Figure 23, consists of two loops. The first loop is a photonically filtered OEO loop produces stable microwave or millimeter-wave output at a range of RF frequencies corresponding to a harmonic of the etalon free spectral range (*n*×*FSR)*. The second loop uses the Pound-Drever-Hall method[42] for frequency stabilization of the seed CW laser source to the Fabry-Perot etalon.

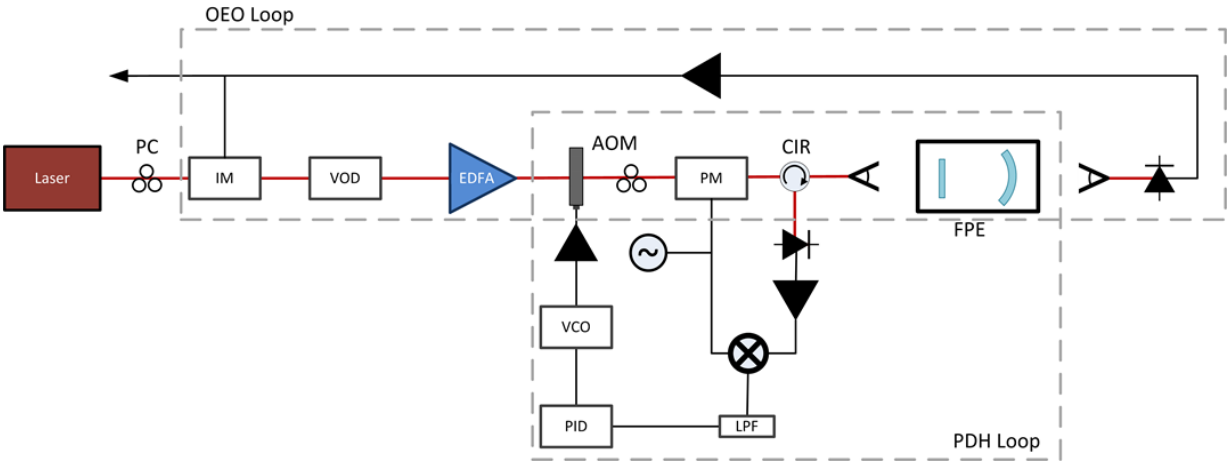

Figure 23. Setup for optoelectronic oscillator with Pound-Drever-Hall frequency stabilization – PC, Polarization controller; IM, Intensity modulator; VOD, Variable optical delay; EDFA, Erbium-doped fiber amplifier; AOM, Acousto-optic modulator; PM, Phase modulator; CIR, Circulator; FPE, Fabry-Perot etalon; LPF, Low pass filter; PID, Proportional-integral-derivative controller; VCO, Voltage-controlled oscillator.

Pound-Drever-Hall Frequency Stabilization

The laser is a commercially available, 1 kHz linewidth fiber laser. Ambient temperature variations cause the output optical frequency to drift several megahertz per minute, thus the laser must be frequency locked to the etalon for OEO operation.

For PDH correction, the laser first propagates through an acousto-optic modulator (AOM) for fast feedback to the optical frequency. A phase modulator generates sidebands before the beam is free-space coupled to the etalon face. As shown in Figure 23, the AOM and PM are both contained within the OEO loop and do not negatively affect microwave phase noise. As with traditional PDH frequency correction, the return signal from the etalon is detected, mixed with the PM driving frequency. The resulting error signal is a proportional to the frequency difference between the input laser and the center of the FP resonance[43]. The error signal is then low pass filtered, and used for feedback to the AOM via a proportional-integral-derivative (PID) controller and voltage controlled oscillator (VCO). The AOM provides fast feedback to the laser frequency for linewidth narrowing but has limited dynamic range. Feedback to the laser cavity length provides slower, but larger dynamic range to ensure long term operation.

The PDH loop keeps the laser frequency stabilized to the center of an etalon resonance which reduces frequency drift as well as significantly narrowing its linewidth. Indeed, systems locked to similarly constructed etalons have been shown to produce laser linewidths less than a 1 Hz[44, 45].

The narrow linewidth and frequency stability provided by the PDH lock benefit the microwave generated signal in several ways. When using a photonic filter in an OEO cavity, the laser linewidth should be narrow as compared to the filter bandwidth to avoid

transfer of optical frequency fluctuations onto the microwave tone[36]. Even if the linewidth is narrow with respect to the etalon resonance, long term drift of the optical frequency within the etalon resonance causes a time-varying phase shift from the transfer function of the etalon. This effect has been shown to produce frequency variations in the RF tone[47].

Another study on the effects of chromatic dispersion on OEO phase noise[48] showed that phase fluctuations, δψ are related to both the chromatic dispersion of the optical fiber D_λ, as well as the optical frequency fluctuations δυ:

$$\delta\psi = 2\pi f_0 \lambda_0^2 D_\lambda \frac{L}{c} \delta\nu. \tag{15}$$

The work showed near 10 dB improvement in OEO phase noise by using zero dispersion fiber instead of SMF28 (for a 4 km length). Thus minimization of frequency noise is important for long loop lengths.

Optoelectronic Oscillator Loop

The laser enters the OEO loop at the intensity modulator (IM) and passes through a variable optical delay (VOD). The VOD consists of a short, free space optical delay and is the point in the loop at which long, kilometer lengths of fiber may be added to lengthen the OEO loop. The free-space section is used to control the loop length such that the OEO fundamental frequency matches with a multiple of the etalon FSR.

After the VOD, the signal passes through an erbium-doped fiber amplifier (EDFA). This optical amplification is necessary to overcome significant optical losses in the loop coming from the IM, PM, AOM, and imperfect etalon coupling while still maintaining

sufficient optical power on the photodiode. The beam is then frequency corrected before passing through the etalon. A photodiode detects the signal after transmission through the etalon. It then passes through an RF amplifier before being split with a 3 dB coupler for output at one port and the other the return to the IM to complete the loop.

The Fabry-Perot etalon used here consists of an ultralow expansion quartz spacer with optically contacted fused silica end mirrors. It is held in a vacuum chamber atop an active vibration isolation optical table. The FSR of the etalon is 1.50 GHz with a finesse of 100,000, giving transmission peaks of ~15 kHz FWHM. A comparison of the filtering of this etalon and that used in work by Ozdur et al. is shown in Figure 24. The etalon used previously had 10.287 GHz FSR and 1,000 finesse, for resonance widths of 10.287 MHz. As the plot shows, the filter used here is almost three orders of magnitude narrower than the one used previously. It provides 20 dB suppression at 100 kHz offset and 40 dB suppression at 1 MHz offset.

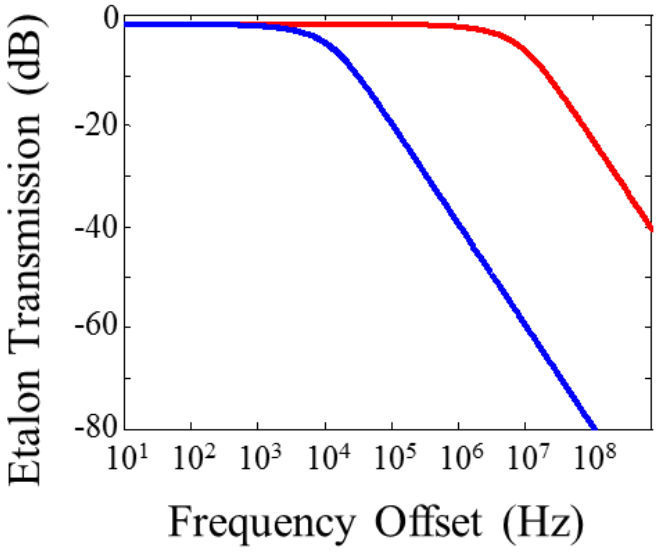

Figure 24 Filtering comparison of current etalon (blue) against previously used etalon (red).

Tunability

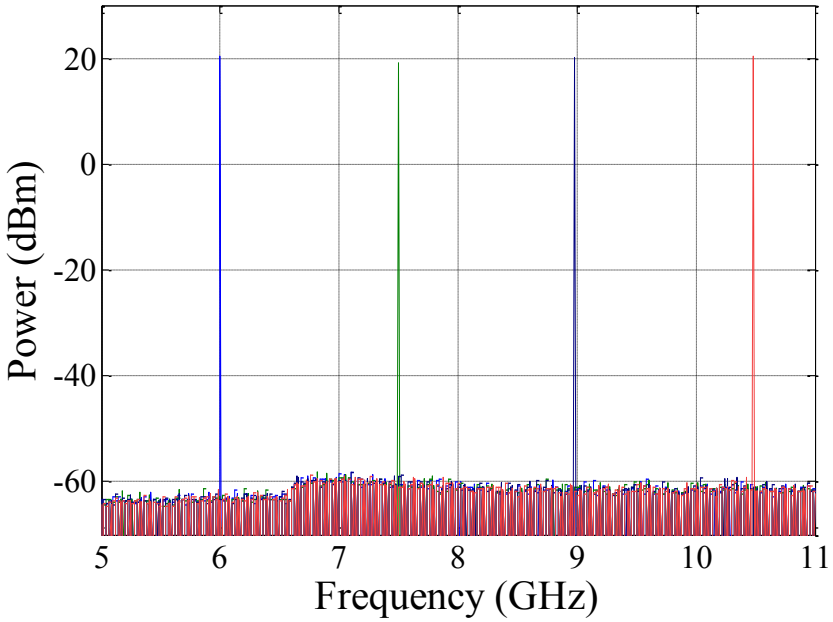

Figure 25. Overlaid RF spectra displaying oscillation at harmonics of the etalon FSR obtained by tuning of the variable optical delay. Each trace shows single mode operation with no visible spurious modes above the noise floor of the RF spectrum analyzer.

Figure 25 shows single mode operation at 6 GHz, 7.5 GHz, 9 GHz, and 10.5 GHz, each obtained by simple tuning of a free space variable optical delay to align the cavity modes with the etalon resonances. For longer loop lengths (>2 km), OEO modes commonly align more than one etalon resonance, causing operation to be determined by gain competition. For wide band amplifiers or small free spectral range etalons, supplemental RF filters should be added to avoid noise bumps at neighboring etalon resonances, however the RF filter bandwidth requirements are significantly reduced.

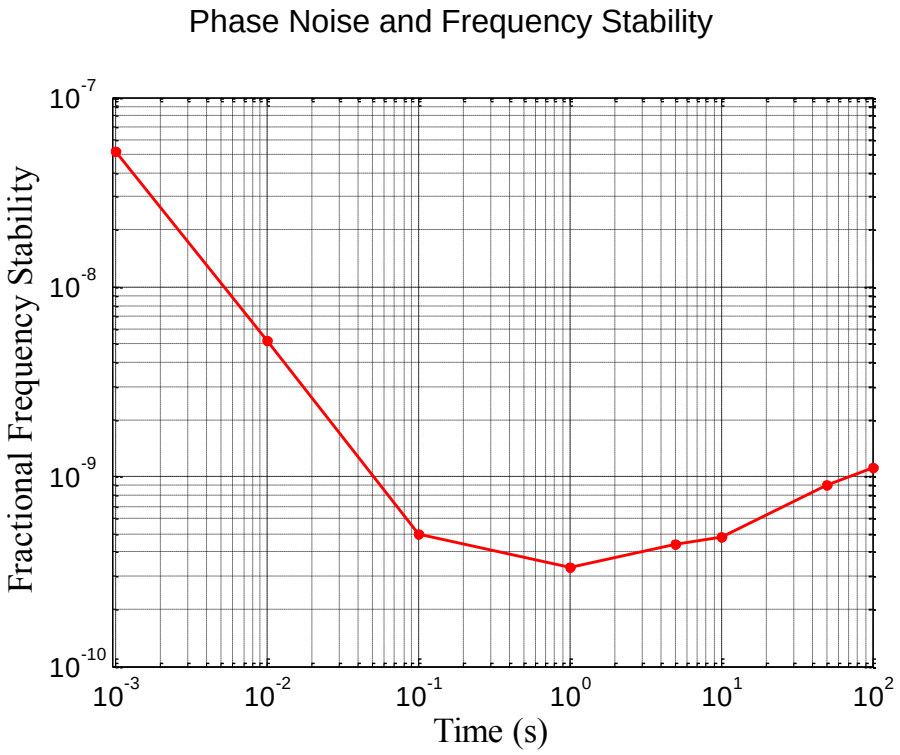

Figure 26. Fractional frequency stability of the 10.5 GHz OEO tone. Frequency stability is 3.3×10^{-10} at 1 s offset.

Figure 26 shows the Allan deviation measurement for the OEO system operating at 10.5 GHz. This result was obtained using off-the-shelf, lower bandwidth modulator, detector, and RF amplifiers. The Allan deviation was measured with no added fiber delay to be 3.3×10^{-10} at 1 second offset.

Phase noise was measured by mixing the 10.5 GHz OEO tone with a 10.24 GHz Poseidon oscillator tone and measuring the resulting 260 MHz tone against a low noise synthesizer. Phase noise with no added delay (blue), 1 km delay (red), and 2 km delay (green) are shown in Figure 27. A phase noise of -120 dBc/Hz at 10 kHz was achieved with 2 km of delay with no spurious modes visible above the noise floor for any of the

delays used. The measurement is limited at offsets above 100 kHz by the reference synthesizer.

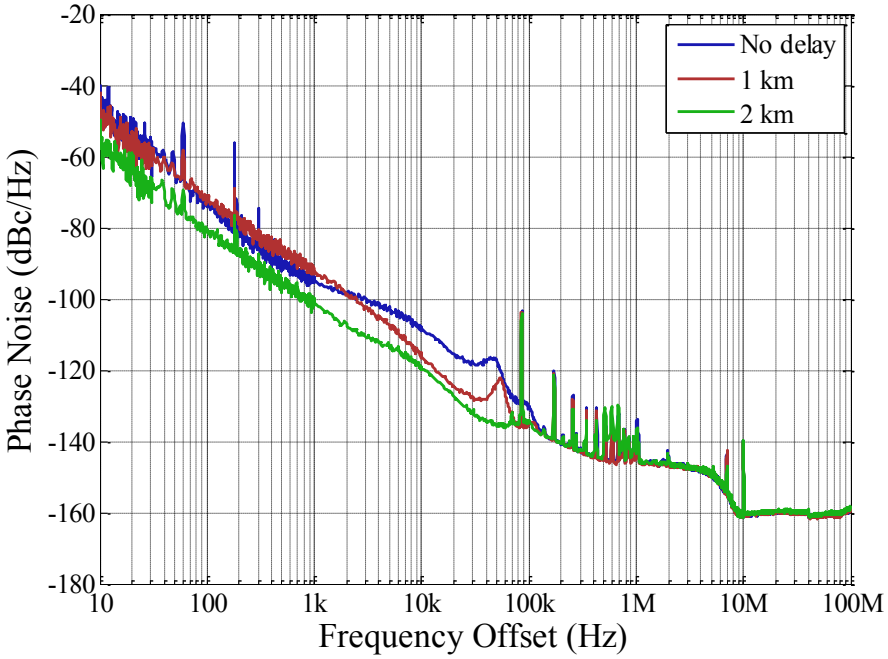

Figure 27. Phase noise for OEO at 10.5 GHz (blue), with 1 km (red) and 2 km (green) of added optical fiber shown. Phase noise at 10 kHz offset is measured at -120 dBc/Hz for the 2 km case with no spurious modes visible above the measurement noise floor. Tones at 84 kHz and harmonics are present on the reference synthesizer signal.

The filtering capability of the etalon was tested by inserting a 23 km fiber delay into the loop. Gain competition forced oscillation at 7.5 GHz and the phase noise was measured directly against a low noise synthesizer. The plot in Figure 28 shows a measurement limited phase noise across the measurement range aside from the spurious tones at 8.45 kHz and harmonics. The tone at 8.6 kHz is suppressed to -90 dBc/Hz.

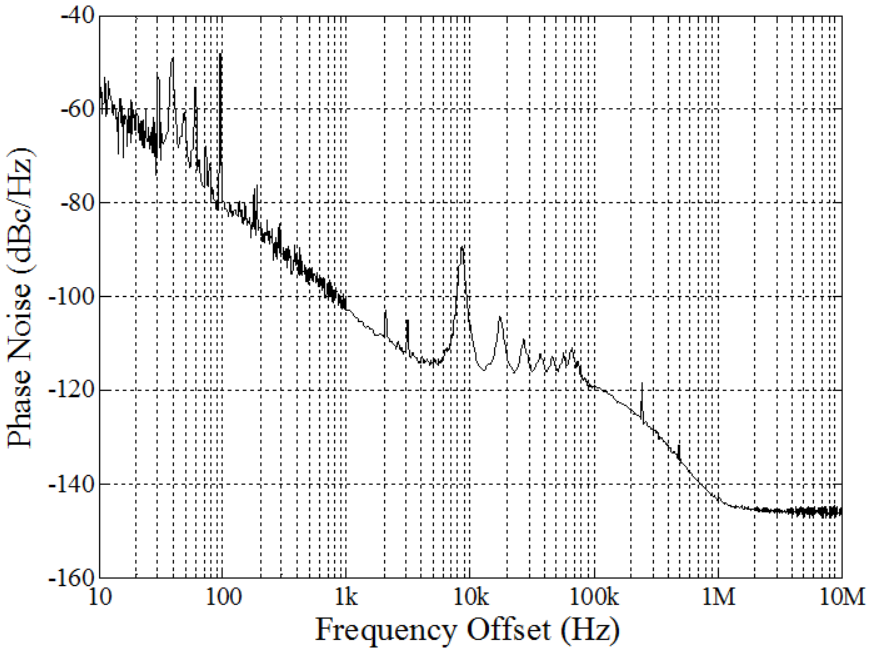

Figure 28. Phase noise spectrum of OEO tone at 7.5 GHz with 23 km of optical fiber delay. Measured against HP 8663A. The phase noise is measurement limited across the measurement range except for the spurious tones at 8.45 kHz and harmonics, the first of which is suppressed to -90 dBc/Hz.

High Frequency Background

Operation of OEOs at high frequency is limited by available modulators and photodiodes with sufficient bandwidth to sustain oscillation. Several novel, high bandwidth modulators have been investigated for use in OEOs. In 2002, Chang et al.[49] showed a 39 GHz OEO using a polymer-based electrooptic modulator and in 2006, an electroabsorption modulator was used for oscillation at 40 GHz while generating pulses directly out of the system[50]. Recently, a whispering gallery mode resonator was used to filter spurious modes, as an optical storage element, and to replace the electro-optic modulator to produce a 34.7 GHz tone[51]. As an alternative to creating high bandwidth modulators,

frequency multiplication has been used to generate high frequency signals from low bandwidth modulators[52,53] including an OEO based on a reciprocating optical modulator to produce a 52.8 GHz millimeter-wave signal with the modulator oscillating at 4.4 GHz[54].

Phase noise measurements for these systems have proven challenging. High frequency reference sources and measurement equipment are not currently widespread. Thus measurements are largely limited by noise added during the process of downconverting the signal to a frequency that can be measured on standard equipment. The most notable result among the previously mentioned works is from the electroabsorption modulator which was limited by the reference oscillator to -100 dBc/Hz at 10 kHz offset.

Recent improvements in fabrication and RF components have made modulators, detectors and amplifiers commercially available at up to 100 GHz. This work uses a lithium niobate ($LiNbO_3$) intensity modulator and a photodiode with bandwidths of 70 GHz as well as RF amplifiers in the ranges of 10 GHz, 35 GHz, and 55 GHz. Using this setup, we show OEO operation at 1.5 GHz harmonics of the etalon FSR as high as 60 GHz.

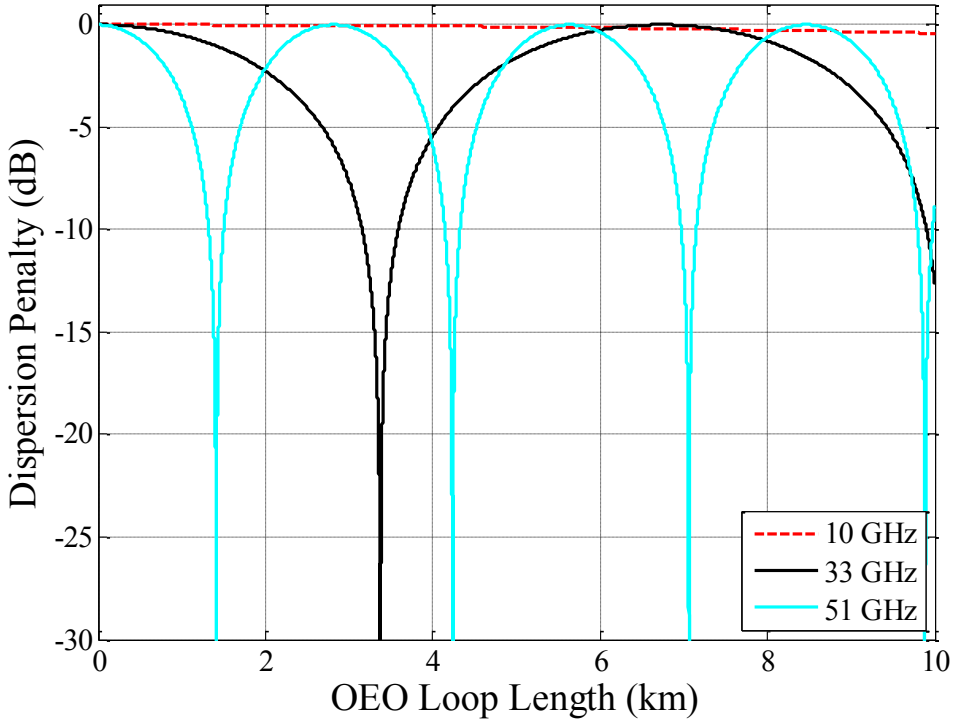

Figure 29. Dispersion penalty for intensity modulated signals at 10 GHz (red), 33 GHz (black), and 51 GHz (cyan). While the 10 GHz tone was relatively unaffected, fiber lengths of 4.5 km and 3 km were chosen to reduce loss for the respective 33 GHz and 51 GHz signals.

The effect of power fading, found in uncompensated, long distance photonic links becomes an issue for high frequency OEO operation[49,55]. Chromatic dispersion in the optical fiber causes different phase shifts in the upper and lower intensity modulated sidebands which dephase over several kilometers. The partial conversion of intensity modulation to phase modulation causes loss at the detector. Figure 29 shows the power fading effect for different operating frequencies used in this work as calculated from the expression:

$$\cos\left(\frac{1}{2}\beta_2\omega^2 L\right), \tag{16}$$

where β_2 is the dispersion in standard single mode fiber, ω the microwave frequency, and L is the length of the OEO loop. The graph shows that while a 10 GHz tone is relatively unaffected for standard single-mode fiber delays shorter than 10 km, fiber length considerations must be made for the 33 GHz and 51 GHz loops. To minimize losses, fiber lengths for these setups were chosen to be 4.5 km (3 dB loss) and 3 km (0.1 dB loss), respectively. Longer fiber lengths may be chosen at successive maxima on the dispersion penalty plot to increase optical storage time while avoiding loss. The lengths chosen for this work were to maintain spurious mode suppression and minimize long term frequency fluctuations due to fiber length change. Decorrelation between the carrier and sidebands is not expected to contribute significantly to the microwave phase noise, even for long fiber delays due to the laser's long coherence length (~200 km).

High Frequency Results

At high oscillation frequencies, the modulator and photodetector were replaced with 70 GHz bandwidth models. RF amplifiers in the range of 35 and 55 GHz were used along with 1.85 mm cables. Figure 30 shows the RF spectrum of the 33 GHz tone using 4.5 km of optical fiber delay to minimize the power fading effect.

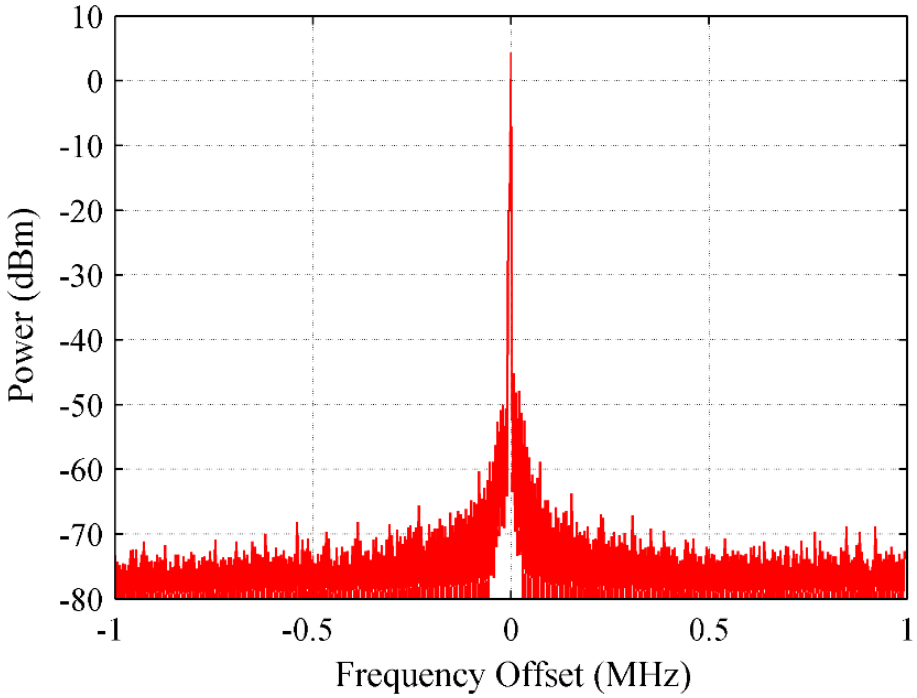

Figure 30. RF spectrum of OEO operating at 33.0 GHz with 4.5 km of fiber delay added (RBW = 1 kHz).

The measurement is instrument floor limited at high frequency offsets with a phase noise of -92 dBc/Hz at 10 kHz offset and no visible OEO spurious modes above the noise floor.

Using the high frequency electronic amplifiers, intensity modulator, photodiode, and cables, millimeter wave tones were generated at harmonics of 1.5 GHz in the range of 51 to 60 GHz. Signals at such high frequency can be difficult to measure with standard, lower bandwidth laboratory equipment. A harmonic mixer (Agilent M1970V) was used to generate a 5th harmonic of the 10.24 GHz Poseidon Oscillator tone to downconvert the 51 GHz OEO tone for measurement against a low noise synthesizer.

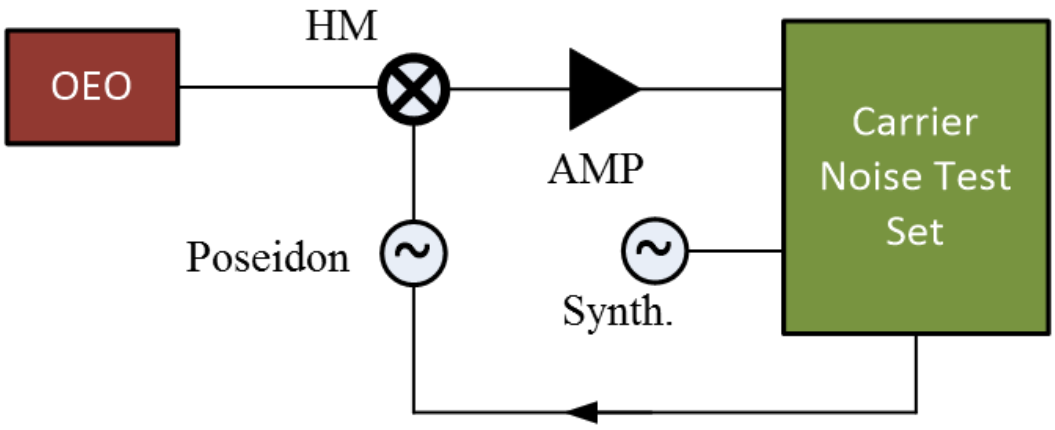

Figure 31. Configuration for high frequency phase noise measurement. The Poseidon oscillator tone at 10.24 GHz is multiplied up to its fifth harmonic at 51.20 GHz and mixed with the 51 GHz tone within the harmonic mixer (HM). The resulting 200 MHz must be amplified with a low noise, 30 dB RF amplifier (AMP) before measuring against a low noise tunable synthesizer (Synth.)

The low phase noise Poseidon oscillator was chosen over a higher noise tunable synthesizer to minimize the phase noise of the generated 5th harmonic reference signal. However its output tone is fixed at 10.24 GHz. Due to the lack of tunability of the reference, and the significantly higher loss at the generated 6th harmonic from the mixer, the 51 GHz tone was the only choice in an appropriate frequency range and power level for phase noise measurement. Figure 32 shows the measured phase noise of the 51 GHz millimeter-wave tone with an added delay of 3 km of SMF. The low frequency tone out of the mixer required 30 dB of amplification after the mixing process due to low conversion efficiency and cable losses. Phase noise of -105 dBc/Hz was measured at 10 kHz offset.

Several artifacts are present on the phase noise plot. Tones at 3 kHz and harmonics, not observed at lower operating frequencies, are thought to be a result of the mixing process, though this could not be verified with the measurement equipment

available. Tones at 84 kHz and harmonics are present on the Poseidon oscillator tone before input into the harmonic mixer. A single spurious mode of the OEO is visible above the noise floor at 68.5 kHz which was amplified by the measurement setup to -99 dBc/Hz.

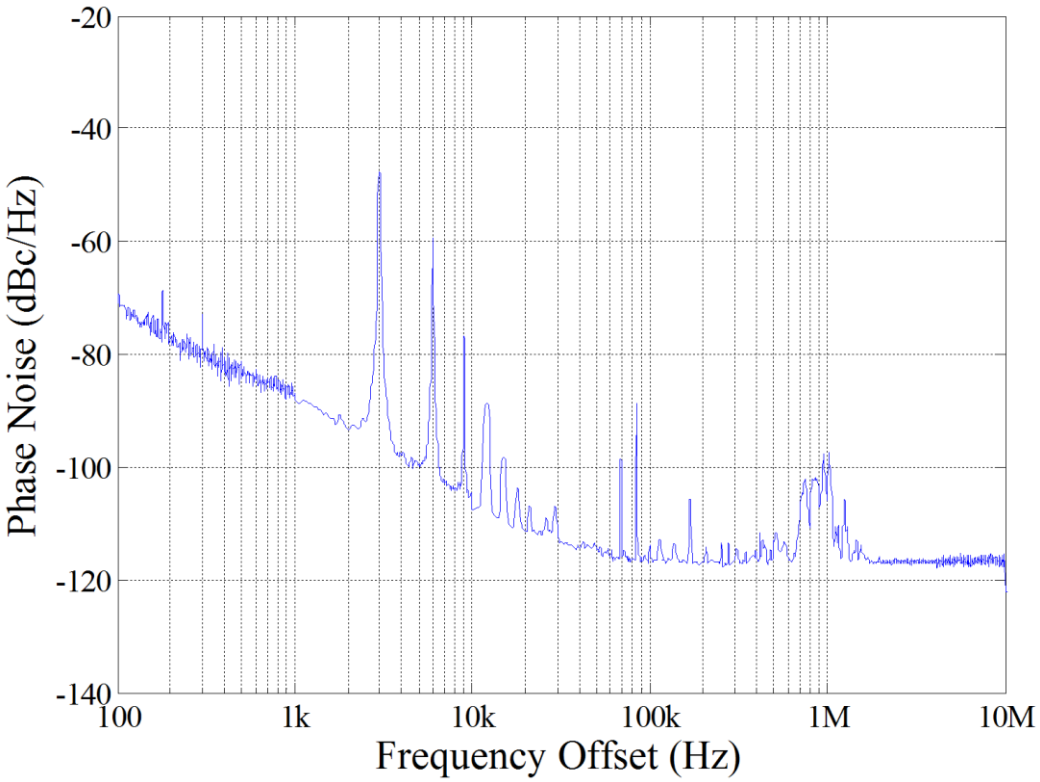

Figure 32. Measured phase noise for 51.0 GHz millimeter-wave tone. The phase noise of -105 dBc/Hz at 10 kHz is limited by the measurement. A single OEO spurious mode is visible at 68.5 kHz offset, amplified to -99 dBc/Hz by a signal amplifier. Artifacts at 3 kHz and harmonics and 84 kHz and harmonics are from the mixing process.

With the long optical delays removed to enable tuning of the oscillation frequency, millimeter-wave tones were produced as high as 60 GHz. The millimeter-wave tone was out of range for the harmonic mixer and 10 GHz reference source to produce an RF tone for diagnostics at low frequencies. However, the high resolution optical spectrum trace (Agilent 8164B), shown in Figure 33 clearly demonstrates oscillation at 60 GHz with the

carrier and upper sideband displayed. To the authors' knowledge this is the highest reported frequency produced by an OEO.

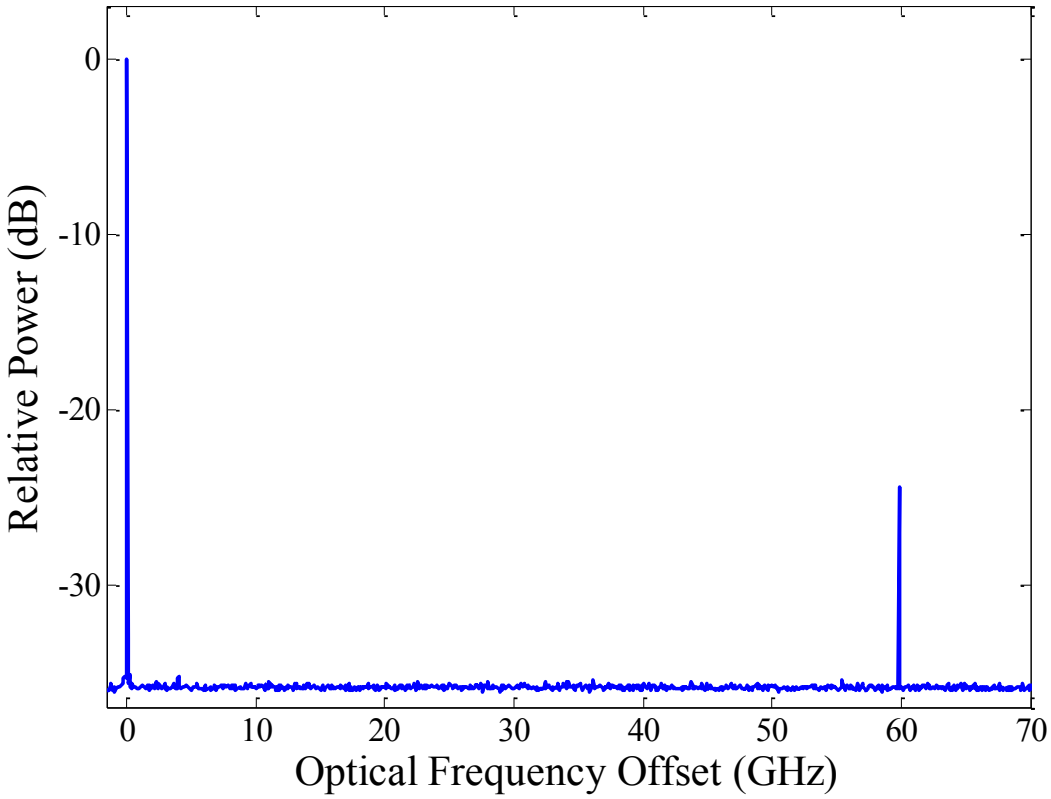

Figure 33. High resolution optical spectrum of OEO operating at 60 GHz. The carrier frequency is 193.4 THz. (RBW = 75 MHz).

CHAPTER 4: SPURIOUS MODE SUPPRESSION COMPARISON AND FUTURE WORK

The narrow filtering of a high finesse etalon allows for a single loop oscillator with very long loop length while sustaining low spurious mode levels. This section compares etalon mode suppression with dual loop configurations.

The spurious mode pattern of a single loop OEO can be modeled by the expression[34]

$$\left|1 - A(\omega)e^{i\omega\tau}\right|^{-2} \cdot \omega^{-1/2}, \tag{17}$$

where $A(\omega)$ is the filter transmission function. An etalon transmission can be described by

$$A(\omega) = \frac{(1-r)^2}{1+r^2-2r\cos\delta}, \tag{18}$$

where r is the reflectivity of the (identical) end mirrors and δ is described by

$$\delta = \frac{2\pi}{\lambda} 2nl\cos\theta = \frac{2\pi f}{f_{fsr}}, \tag{19}$$

where the equation has been simplified using $n=1$ (index of vacuum between etalon spacers), $\cos(\theta) = 1$ (laser at normal incidence to etalon), and $f_{fsr}=2nl/c$, the etalon free spectral range. An RF filter can be described by

$$A(\omega) = \frac{\omega_0}{\omega_0 - i\omega}, \tag{20}$$

where $\omega_0=2\pi f_0$ and f_0 is the filter's HWHM transmission spectra. For a dual loop OEO, the filter function can be described by

$$\left|1 - A(\omega)\left[e^{i\omega\tau_1} + e^{i\omega\tau_2}\right]/2\right|^{-2} \cdot \omega^{-1/2}, \quad (21)$$

where $\omega=2\pi f$, and $\tau_{1,2}$ are the fiber delay times.

Using the above expressions, comparisons can be made between the dual loop, RF filter and single loop, etalon filtered OEO spurious modes. Figure 34 shows several cases of filtering with various loop lengths as compared to the Fabry-Perot etalon. The primary loop in all cases is 10 km while the secondary loop is varied for the dual loop plots. The plots are vertically offset to compare the spurious mode locations and heights. An RF filter with a FWHM of 10.24 MHz is used in all cases except for the etalon filtered (blue). This filter bandwidth is typical of high quality, commercially available RF filters near 10 GHz center frequency.

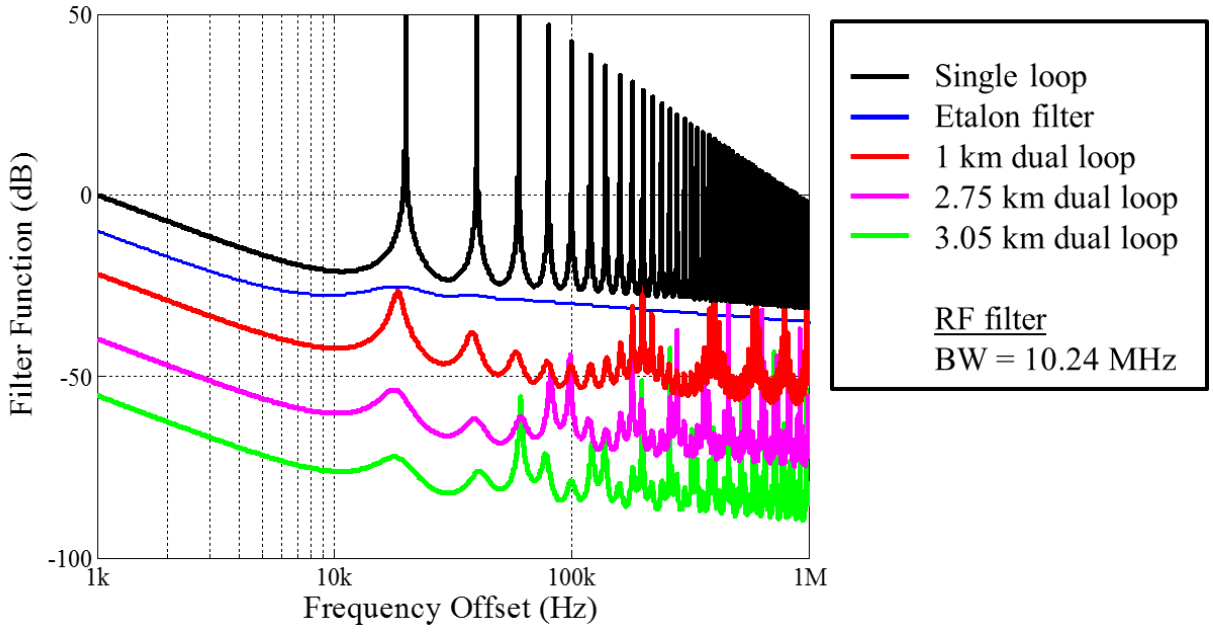

Figure 34. Filter functions of several OEO configurations each with a primary loop of 10 km. All but etalon filtered (blue) use an RF filter bandwidth of 10.24 GHz FWHM.

As can be seen from Figure 34, as the secondary loop length increases in a dual loop OEO the spurious modes closest to the carrier are suppressed. However, increasing the secondary loop length also lowers the offset frequency at which the secondary loop modes, which see less suppression, occur.

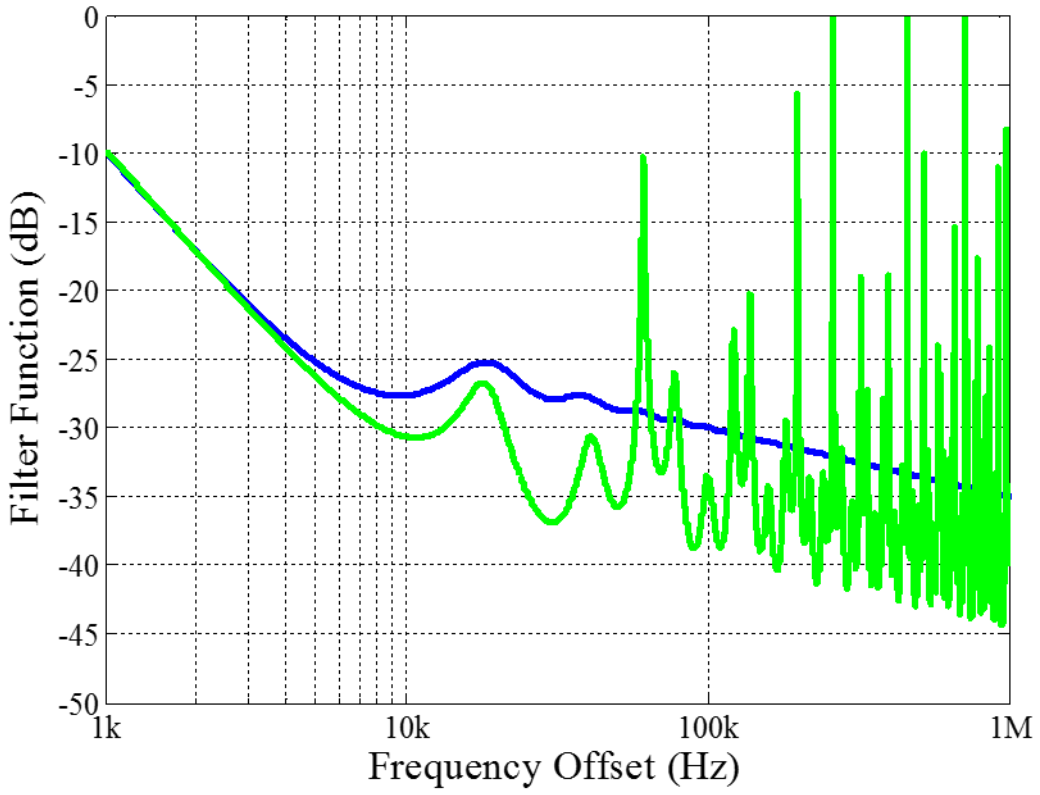

Figure 35. Comparison of etalon filtered OEO (blue) with dual loop, 3.05 km secondary delay, 10.24 MHz RF filter OEO (green).

Comparing the etalon filtering with longer length dual loops (Figure 35) shows an interesting result. With very long secondary loop lengths, the first spurious mode can be suppressed below the level achievable by the etalon in a single loop configuration. However, the suppression is not maintained at higher frequencies. By adding a second fiber loop within the etalon filtered OEO, the close-in modes can be further suppressed

while the etalon's high rejection at higher offset frequencies (Figure 24) can suppress modes arising from a long secondary loop length. This combination of filtering is shown in Figure 36. Addition of the secondary loop further suppresses the first spurious mode by 4 dB while the etalon filtering maintains low spurious mode levels at higher offsets.

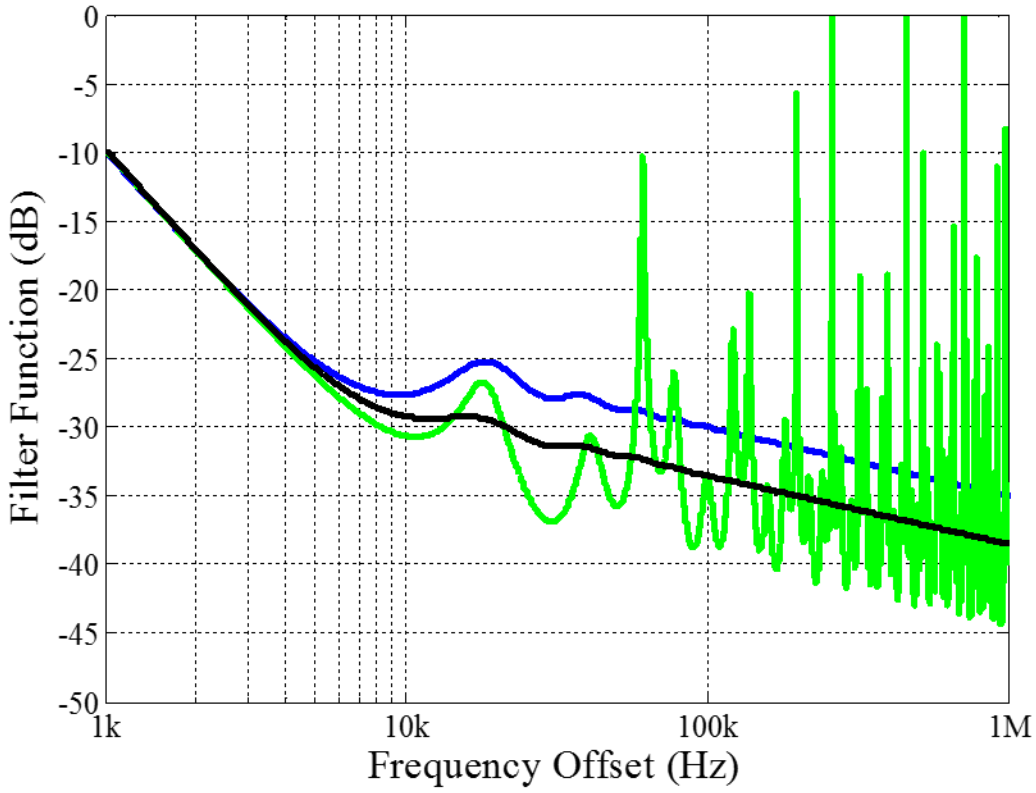

Figure 36. Overlay of dual loop, etalon filtered OEO (black) with 10 km primary loop, 3.1 km secondary loop, and 10.24 MHz RF filter. Etalon filtered (blue) and dual loop (green) OEOs are shown for comparison.

APPENDIX: MULTIHETERODYNE CROSS-CORRELATION

Starting with Eqn. (4), the total electric-field of a laser, taken to be a delta function, and a band-limited incoherent source:

$$E_{tot} = 2A\cos\left(2\pi\nu_L t + \phi_L\right) + 2\sum_{n=n_0}^{n_0+N}\left|q_n\right|\cos\left(\frac{2\pi n}{\tau}t + \phi_n\right) \tag{A.1}$$

The heterodyne part of the voltage across the photodetector resistor[9] is given by

$$V^{(1)}(t) = \Re R_L\sqrt{P_L}\sum_n\sqrt{P_n}\cos\left[2\pi\left(\frac{n}{\tau}-\nu_L\right)t + \left(\phi_n - \phi_L\right)\right], \tag{A.2}$$

with the delayed signal given by

$$V^{(2)}(t) = \Re R_L\sqrt{P_L}\sum_n\sqrt{P_n}\cos\left[2\pi\left(\frac{n}{\tau}-\nu_L\right)t + \left(\phi_n - \phi_L\right) + \frac{2\pi n}{\tau}\Delta t_{ase} - 2\pi\nu_L\Delta t_L\right]. \tag{A.3}$$

The cross-correlation is easily computed in the frequency domain by:

$$S_{1,2}(t) = \mathrm{F}^{-1}\left\{\left[\overline{V^{(1)}(f)}\right]\bullet V^{(2)}(f)\right\}. \tag{A.4}$$

Where the Fourier transform of the time domain voltage signals are given by

$$V^{(1)}(f) = \Re R_L\sqrt{P_L}\sum_n\sqrt{P_n}\left(e^{i(\phi_n-\phi_L)}\delta\left[2\pi\left(f-\frac{n}{\tau}+\nu_L\right)\right] + \left\{e^{-i(\phi_n-\phi_L)}\delta\left[2\pi\left(f+\frac{n}{\tau}-\nu_L\right)\right]\right\}\right) \tag{A.5}$$

and

$$V^{(2)}(f) = \Re R_L\sqrt{P_L}\sum_n\sqrt{P_n}\left(e^{i(\phi_n-\phi_L)}e^{i\frac{2\pi n}{\tau}\Delta t_{ase}}e^{-i2\pi\nu_L\Delta t_L}\delta\left[2\pi\left(f-\frac{n}{\tau}+\nu_L\right)\right]+\right)\ldots$$
$$\left\{e^{-i(\phi_n-\phi_L)}e^{-i\frac{2\pi n}{\tau}\Delta t_{ase}}e^{i2\pi\nu_L\Delta t_L}\delta\left[2\pi\left(f+\frac{n}{\tau}-\nu_L\right)\right]\right\}\Bigg). \tag{A.6}$$

Carrying out the multiplication of the yields:

$$S_{1,2}(t) = \mathrm{F}^{-1}\left\{2\Re^2 R_L^2 P_L \sum_n P_n \left(e^{i\frac{2\pi n}{\tau}\Delta t_{ase}} e^{-i2\pi\nu_L \Delta t_L} \delta\left[2\pi\left(f - \frac{n}{\tau} + \nu_L\right)\right] + \right.\right. \ldots$$
$$\left.\left. \left\{ e^{-i\frac{2\pi n}{\tau}\Delta t_{ase}} e^{i2\pi\nu_L \Delta t_L} \delta\left[2\pi\left(f + \frac{n}{\tau} - \nu_L\right)\right]\right\}\right)\right\} \quad \text{(A.7)}$$

Notice that the phases, φ_L and φ_n, drop out of the equation. Carrying out the Fourier transform gives the heterodyne cross-correlation result:

$$S_{1,2}(t) = 4\Re^2 R_L^2 P_L \sum_n P_n \cos\left[2\pi\left(\frac{n}{\tau} - \nu_L\right)\left(t + \Delta T + \Delta t_{ase}\right) + 2\pi\nu_L\left(\Delta t_{ase} - \Delta t_L\right)\right]. \quad \text{(A.8)}$$

Here we have defined ΔT to be the difference in the paths common to both Δt_{ase} and Δt_L. As stated in Section [2], the multiheterodyne cross-correlation may be taken as a superposition of heterodyne signals which do not overlap in frequency. For a set of m heterodyne components, the cross-correlation is given by:

$$S_{1,2}(t) = 4\Re^2 R_L^2 P_L \sum_m \sum_n P_n \cos\left[2\pi\left(\left(\frac{n}{\tau} + mf_{\mathrm{fsr}}\right) - \left(\nu_L + mf_{rep}\right)\right)\left(t + \Delta T + \Delta t_{ase}\right) + \ldots\right.$$
$$\left. 2\pi\left(\nu_L + mf_{rep}\right)\left(\Delta t_{ase} - \Delta t_L\right)\right] \quad \text{(A.9)}$$

where f_{fsr} is the etalon free spectral range, and f_{rep} is the laser repetition rate. By rearranging terms, we can see that the correlation can be written as

$$S_{1,2}(t) = 4\Re^2 R_L^2 P_L \sum_m \sum_n P_n \cos\left[2\pi\left(\frac{n}{\tau} - \nu_L\right)\left(t + \Delta T + \Delta t_{ase}\right) + \ldots\right. \quad \text{(A.10)}$$

$$2\pi\nu_L\left(\Delta t_{ase}-\Delta t_L\right)+m\left[2\pi\delta_{det}\left(t+\Delta T+\Delta t_{ase}\right)+2\pi f_{rep}\left(\Delta t_{ase}-\Delta t_L\right)\right]\Bigg]$$

where $\delta_{det}= f_{fsr} - f_{rep}$. By setting $\Delta t_L = 0$ and taking the sum of cosines we obtain

$$S_{1,2}\left(t\right)=4\Re^2R_L^2P_L\left[\frac{\sin\left(m\alpha\right)}{\sin\left(\alpha\right)}\right]\sum_n P_n\cos\left(\varphi\right) \tag{A.11}$$

with φ and α given by

$$\varphi=2\pi\left(\frac{n}{\tau}-\nu_L+(m-1)\frac{\delta_{\mathrm{det}}}{2}\right)\left(t+\Delta T+\Delta t_{ase}\right)+2\pi\left(\nu_L+(m-1)\frac{f_{rep}}{2}\right)\Delta t_{ase} \tag{A.12}$$

and

$$\alpha=\pi\delta_{\mathrm{det}}\left(t+\Delta T\right)+\pi f_{fsr}\Delta t_{ase} \tag{A.13}$$

LIST OF REFERENCES

1 J. Ye and S. Cundiff, *Femtosecond Optical Frequency Comb: Principle, Operation, and Applications,* New York: Springer Verlag, 2005.

2 I. Coddington, W. C. Swann, and N. R. Newbury, “Coherent Multiheterodyne Spectroscopy Using Stabilized Optical Frequency Combs,” Phys. Rev. Lett., vol. 100, no. 013902, (2008).

3 D. Mandridis, I. Ozdur, F. Quinlan, M. Akbulut, J. J. Plant, P. W. Juodawlkis, and P. J. Delfyett, “Low-noise, low repetition rate, semiconductor-based mode-locked laser source suitable for high bandwidth photonic analog-digital conversion,” Appl. Opt., vol. 49, no. 15, (2010).

4 M. Akbulut, S. Bhooplapur, I. Ozdur, J. Davila-Rodriguez, and P. J. Delfyett, ”Dynamic line-by-line pulse shaping with GHz update rate,” Opt. Exp., vol. 18, no. 17, pp. 18284-18291, (2010).

5 G. G. Yeas, F. Quinlan, S. A. Diddams, S. Osterman, S. Mahadevan, S. Redman, R. Terrien, L. Ramsey, C. F. Bender, B. Botzer, S. Sigurdsson, “Demonstration of On-Sky Calibration of Astronomical Spetctra using a 25 GHz near-IR Laser Frequency Comb” Opt. Exp., vol. 20, no. 6, pp. 6631-6643, (2012).

6 I. Coddington, W. C. Swann, L. Nenadovic, and N. R. Newbury, “Rapid and precise absolute distance measurements at long range,” Nature Photon., vol. 3, pp. 351- 356, 2009.

7 X. S. Yao and L. Maleki, “Optoelectronic microwave oscillator,” J. Opt. Soc. Am. B, vol. 13, pp. 1725-1734, August 1996.

8 D. Eliyahu, D. Seidel, and L. Maleki, “RF Amplitude and Phse-Noise Reduction of an Optical Link and an Opto-Electronic Ocsillator,” IEEE Trans. Microw. Theory Tech., vol. 56, no. 2, (2008).

9 M. Bagnell, J. Davila-Rodriguez, A. Ardey, and P. J. Delfyett, “Dispersion Measurements of a 1.3 μm Quantum Dot Semiconductor Optical Amplifier over 120 nm of Spectral Bandwidth,” Appl. Phys. Lett., **96**, pp. (211907) 1-3, 2010.

10 P. Hlubina, “White-Light Spectral Interferometry with the Uncompensated Michelson Interferometer and the Group Refractive Index Dispersion in Fused Silica,” Opt. Comm., **193**, pp. 1-7, 2001.

11 S. Diddams and Jean-Claude Diels, “Dispersion Measurements with White Light Interferometry,” J. of Opt. Soc. B, **13**, pp. 1120-1129, 1996.

12 L. Lepetit, G. Cheriaux, and M. Joffre, “Linear Techniques of Phase Measurement by Femtosecond Spectral Interferometry for Applications in Spectroscopy,” J. of Opt. Soc. B, **12**, pp. 2467-2474, 1995.

13 E. U. Rafailov, M. A. Cataluna, and W. Sibbett, “Mode-Locked Quantum Dot Lasers,” Nat. Photon., **1**, pp. 395-401, 2007.

14 P. Delfyett, S. Gee, M. T. Choi, H. Izadpanah, W. Lee, S. Ozharar, F. Quinlan, T. Yilmaz, “Optical Frequency Combs for Semiconductor Lasers and Applications in

Ultrawideband Signal Processing and Communications," J. of Lightw. Tech. **24**, pp. 2701-2119, 2006.

15 Y. Deng, Z. Wu, L. Chai, Ching-yue Wang, K. Yamane, R. Morita, M. Yamashita, and Z. Zhang, "Wavelet-Transform Analysis of Spectral Shearing Interferometry for Phase Reconstruction of Femtosecond Optical Pulses," Opt. Expr., **13**, pp. 2120-2126, 2005.

16 Y. Deng, W. Yang, C. Zhou, X. Wang, J. Tao, W. Kong, and Z. Zhang, "Wavelet-Transform Analysis for Group Delay Extraction of White Light Spectral Interferograms," Opt. Expr., **17**, pp. 6038-6043, 2009.

17 K. Naganuma and H. Yasaka, "Group Delay and α-Parameter Measurement of 1.3 μm Semiconductor Traveling-Wave Optical Amplifier Using the Interferometric Method," IEEE J. of Quant. Electron., **27**, pp. 1280-1287 1991.

18 T. Skauli, P. S. Kuo, K. L Vodopyanov, T. J. Pinguet, O. Levi, L. A. Eyres, J. S. Harris, M. M. Fejer, B. Gerard, L. Becouarn, and E. Lallier, "Improved Dispersion Relations for GaAs and Applications to Nonlinear Optics," J. of Appl. Phys., **94**, pp. 6447-6455 2003.

19 I. Coddington, W. C. Swann, and N. R. Newbury, "Coherent multiheterodyne spectroscopy using stabilized optical frequency combs," Phys. Rev. Lett., 100(1), 013902 (2008).

20 A. Schliesser, M. Brehm, F. Keilmann, and D. W. van der Weide, "Frequency-comb infrared spectrometer for rapid, remote chemical sensing," Opt. Express, **13**(22), 9029-9038 (2005).

21 I. Coddington, W. C. Swann, and N. R. Newbury, “Coherent dual-comb spectroscopy at high signal-to-noise ratio,” Phys. Rev. A, 82(4), 043817 (2010).

22 I. Coddington, W. C. Swann, L. Nenadovic, and N. R. Newbury, “Rapid and precise absolute distance measurements at long range,” Nature Photon., 3(6), 351-356 (2009).

23 T. Liu, N. R. Newbury, and I. Coddington, “Sub-micron absolute distance measurements in sub-millisecond times with dual free-running femtosecond Er fiber-lasers,” Opt. Express, 19(19), 18501-18509 (2011).

24 I. Coddington, W. C. Swann, and N. R. Newbury, “Coherent linear optical sampling at 15 bits of resolution,” Opt. Lett., 34(14), 2153-2155 (2009).

25 F. Ferdous, D. E. Leaird, C. B. Huang, and A. M. Weiner, “Dual-comb electric-field cross-correlation technique for optical arbitrary waveform characterization,” Opt. Lett., 34(24), 3875-3877 (2009).

26 F. R. Giorgetta, I. Coddington, E. Baumann, W. C. Swann, and N. R. Newbury, “Fast high-resolution spectroscopy of dynamic continuous-wave laser sources,” Nature Photon., 4(12), 853-857 (2010).

27 M. Bagnell, J. Davila-Rodriguez, C. Williams, and P. J. Delfyett, “Multiheterodyne Detection and Sampling of Periodically Filtered White Light for Correlations at 20 km of Delay,” Phot. Journal, **4**, pp. 504-511, 2012.

28 R. Hanbury Brown and R. Q. Twiss, “Interferometry of the Intensity Fluctuations in Light. I. Basic Theory: The Correlation between Photons in Coherent Beams of Radiation,” Proceedings of the Royal Society A: Mathematical and Physical Sciences, 242(1230), 300-324 (1957).

29 D. Mandridis, I. Ozdur, M. Bagnell, P. J. Delfyett, “Free spectral range measurement of a fiberized Fabry-Perot etalon with sub-Hz accuracy,” Opt. Express, 18(11), 11264(2010).

30 J. Davila-Rodriguez, M. Bagnell, C. Williams, and P. J. Delfyett, “Multiheterodyne Detection for Spectral Compression and Down-Conversion of Arbitrary Periodic Optical Signals,” J. Lightwave Technol., 29(20), 3091-3098 (2011).

31 C. Williams, F. Quinlan, and P. J. Delfyett, “Injection-locked mode-locked laser with long-term stabilization and high power-per-combline,” IEEE Photon. Tehcnol. Lett., 21(2), 94-96 (2009).

32 P. Devgan, “A Review of Optoelectronic Oscillators for High Speed Signal Processing Applications,” ISRN Electronics, v. 2013, 2013.

33 X. S. Yao and L. Maleki, “Multiloop optoelectronic oscillator,” IEEE J. of Quant. Electron., vol. 36, pp. 79-84, January 2000.

34 D. Eliyahu and L. Maleki, “Low phase noise and spurious level in multi-loop opto-electronic oscillators,” Proc. 2003 IEEE International Frequency Control Symposium, pp. 405-410.

35 W. Zhou and G. Blasche, “Injection-locked dual opto-electronic oscillator with ultra-low phase noise and ultra-low spurious level,” IEEE Trans. Microw. Theory Tech., vol. 53, pp. 929-933, March 2005.

36 D. Strekalov, D. Aveline, N. Yu, R. Thompson, A. B. Matsko, and L. Maleki, “Stabilizing an optoelectronic microwave oscillator with photonic filters,” J. Lightw. Technol., 21, 12, (2003).

37 J. Yang, Y. Jin-Long, W. Yao-Tian, Z. Li-Tai, and Y. En-Ze, “An Optical Domain Combined Dual-Loop Optoelectronic Oscillator,” IEEE Phot. Technol. Lett. **19**, pp. 807-809, 2007.

38 A. B. Matsko, L. Maleki, A. A. Savchenkov, and V. S. Ilchenko, “Whispering Gallery Mode Based Optoelectronic Microwave Oscillator,” J. of Modern Opt., **50**, pp. 2523-2542, 2003.

39 J. M. Kim and D. Cho, “Optoelectronic oscillator stabilized to an intra-loop Fabry-Perot cavity by a dual servo system,” Opt. Ex., vol. 18, pp. 14905-14912, June 2010.

40 I. Ozdur, M. Akbulut, N. Hoghooghi, D. Mandridis, M. U. Piracha, and P. J. Delfyett, “Optoelectronic loop design with 1000 finesse Fabry-Perot etalon,” Opt. Lett., 35(6), 799-801 (2010).

41 M. Bagnell, J. Davila-Rodriguez, and P. J. Delfyett, “Millimeter-Wave Generation in an Optoelectronic Oscillator Using an Ultrahigh Finesse Etalon as a Photonic Filter,” J. of Lightwav. Technol. **32**, pp. 1063-1067, 2014.

42 R. W. P. Drever, J. L. Hall, F. V. Kowalski, J. Hough, G. M. Ford, A. J. Munley, and H. Ward, “Laser phase and frequency stabilization using an optical resonator,” Appl. Phys. B, **31**, pp.97-105, (1983).

43 E. D. Black, “An introduction to Pound-Drever-Hall laser frequency stabilization,” Am. J. Phys., **69**(1), 2001.

44 C. Salomon, D. Hils, and J. L. Hall, “Laser stabilization at the millihertz level,” J. opt. Soc. Am. B, **5**, (8), (1988).

45 B. C. Young, F. C. Cruz, W. M. Itano, and J. C. Bergquist, “Visible Lasers with Subhertz Linewidths,” Phys. Rev. Lett., **82**, (19), pp. 3799-3802, (1999).

46 M. Bagnell, J. Davila-Rodriguez, and P. J. Delfyett, “Highly stable optoelectronic oscillator with a 10^5 finesse etalon as a photonic filter,” Avionics, Fiber-Optics and Photonics Technology Conference, 2012.

47 I. Ozdur, D. Mandridis, N. Hoghooghi, and P. J. Delfyett, “Low noise optically tunable opto-electronic oscillator with Fabry-Perot etalon,” J. Lightw. Technol., vol. 28, pp. 3100-3106, November 2010.

48 K. Volyanskiy, Y. K. Chembo, L. Larger, and E. Rubiola, “Contribution of laser frequency and power fluctuations to the microwave phase noise of optoelectronic oscillators,” J. Lightw. Technol., vol. 18, pp. 2730-2735, September 2010.

49 D. H. Chang, H. R. Fetterman, H. Erlig, H. Zhang, M. C. Oh, C. Zhang, and W. H. Steier, “39-GHz Optoelectronic Oscillator Using Broad-Band Polymer Electrooptic Modulator,” IEEE Phot. Technol. Lett., vol. 14, no. 2, pp. 191-193, February 2002.

50 M. Shin, P. S. Devgan, V. S. Grigoryan, P. Kumar, Y. D. Chung, and J. Kim, “Low phase-noise 40GHz optical pulses from a self-starting electroabsorption-modulator-based optoelectronic oscillator,” Optical Fiber Communication Conference, OFB1, March 2006.

51 A. A. Savchenkov, V. S. Ilchenko, J. Byrd, W. Liang, D. Eliyahu, A. B. Matsko, D. Seidel, and L. Maleki,“Whispering-Gallery Mode Based Opto-Electronic Oscillators,” Frequency Control Symposium 2010 IEEE International, pp.554-557. June 2010.

52 Y. Qiao, S. Zheng, H. Chi, X. Jin, and X. Zhang, “A Frequency Doubling Optoelectronic Oscillator Based on a Phase Modulator,” 2012 International Topical Meeting on Microwave Photonics, pp.10-13, 2012

53 L. Wang, N. Zhu, W. Lei, and J. Liu, “A Frequency-Doubling Optoelectronic Oscillator Based on a Dual-Parallel Mach-Zehnder Modulator and a Chirped Fiber Bragg Grating,” IEEE Phot. Technol. Lett., Vol. 23, no. 22, November 2011.

54 T. Sakamoto, T. Kawanishi, and M. Izutsu, “Optoelectronic oscillator employing reciprocating optical modulator for millimeter-wave generation,” Electron. Lett., vol. 43, no. 19, September 2007.

55 U. Gliese, S. Nørskov, and T. N. Nielson, “Chromatic Dispersion in Fiber Optic Microwave and Millimeter-Wave Links,” IEEE Trans. Microw. Theory Techn., vol. 44, no. 10, October 1996.